Natural Resources Canada | Ressources naturelles Canada

GEOLOGICAL SURVEY OF CANADA
OPEN FILE 9201

Major- and trace-element geochemistry of chromite from Alaskan-type ultramafic-mafic intrusions in British Columbia

D. Milidragovic, D.C. Petts, M. Beauchamp, M.J. Polivchuk, and G.T. Nixon

2024

Canada

GEOLOGICAL SURVEY OF CANADA
OPEN FILE 9201

Major- and trace-element geochemistry of chromite from Alaskan-type ultramafic-mafic intrusions in British Columbia

D. Milidragovic[1], D.C. Petts[2], M. Beauchamp[2], M.J. Polivchuk[2], and G.T. Nixon[3]

[1]Natural Resources Canada, Geological Survey of Canada, 1500-605 Robson Street, Vancouver, British Columbia V6B 5J3
[2]Natural Resources Canada, Geological Survey of Canada, 601 Booth Street, Ottawa, Ontario K1A 0E8
[3]British Columbia Geological Survey, Ministry of Energy, Mines and Low Carbon Innovation, Box 9333 Stn Prov Govt, Victoria, British Columbia V8W 9N3

2024

This publication is available for free download through the NRCan Open Science and Technology Repository (https://ostrnrcan-dostrncan.canada.ca/).

Recommended citation
Milidragovic, D., Petts, D.C., Beauchamp, M., Polivchuk, M.J., and Nixon, G.T., 2024. Major- and trace-element geochemistry of chromite from Alaskan-type ultramafic-mafic intrusions in British Columbia; Geological Survey of Canada, Open File 9201, 1 .zip file. https://doi.org/10.4095/p1vd4aw6sj

Publications in this series have not been edited; they are released as submitted by the author.

ISSN 2816-7155
ISBN 978-0-660-73253-4
Catalogue No. M183-2/9201E-PDF
https://doi.org/10.4095/p1vd4aw6sj

ABSTRACT

Magmatic sulfide mineralization in ultramafic-mafic intrusions at convergent margins is becoming an increasingly important global resource of critical metals (Ni-Cu-PGE). In the Canadian Cordillera, a sub-class of convergent margin ultramafic-mafic intrusions, known as Alaskan-type intrusions, occurs in the accreted arc terranes of the North American continental margin. These intrusions have long been recognized for their chromite-associated PGE mineralization. However, their potential to host significant Ni-Cu-PGE sulfide mineralization and their ability to reduce greenhouse gas emissions through permanent carbon mineralization is becoming a focus of current research. This report describes the major and trace element compositions of dunite-hosted Cr-spinel (chromite), measured by Electron Probe Microanalysis (EPMA) and Laser Ablation-Inductively Coupled Plasma-Mass Spectrometry (LA-ICP-MS). These data are part of the effort to better constrain the intrinsic petrological properties of magmas parental to Alaskan-type intrusions and to evaluate their economic potential.

INTRODUCTION

Alaskan-type intrusions are relatively deep-seated magmatic systems emplaced in convergent margin settings. Their potential to host critical metal mineralization (PGEs, i.e., platinum group elements) in association with chromitite has been long recognized (e.g., Nixon et al., 1990; 1997; Johan, 2002; Garuti et al., 2003). These intrusive systems may also contain magmatic sulphide mineralization with high tenors of critical metals: Ni, Cu, Rh, Pt, and Pd, as well as Au (Jackson-Brown, 2017; Milidragovic et al., 2021). The accreted Mesozoic arc terranes of the North American Cordillera are especially well-endowed with these magmatic systems, with several large, well-exposed intrusions located in British Columbia (e.g., Tulameen, Turnagain) and Alaska (e.g., Duke Island). The petrology and economic potential of Alaskan-type intrusions in the Canadian Cordillera remain largely enigmatic despite their well-documented potential for Ni-sulphide (e.g., Turnagain; ~1.8 Mt contained Ni at average grade of 0.21 % Ni; Mudd and Jowitt, 2014) and Pt-alloy (Tulameen; Nixon et al., 1990) mineralization. Recent research, funded through TGI-4, TGI-5, and TGI-6 (e.g., Nixon et al., 2015, 2020a, 2020b; Nott et al., 2020; Milidragovic and Cleven, 2023), put forth a predictive petrological framework for mineralization in Alaskan-type intrusions (Milidragovic et al., 2021). The model, which needs further testing, posits that the mineralization style and potential of Alaskan-type intrusions is largely controlled by the oxidation state and water content of their primary magmas. Moreover, ultramafic rocks are garnering global interest for their potential to reduce the growing CO_2 concentration in the atmosphere through their ability to permanently sequester CO_2 through mineralization reactions (e.g., Kelemen et al., 2019; Power et al., 2020).

This data release contains compositional data for Cr-rich spinel (chromite) from six Alaskan-type intrusions in British Columbia (Fig. 1), determined both by Electron Probe Microanalysis (EPMA) and Laser Ablation-Inductively Coupled Plasma-Mass Spectrometry (LA-ICP-MS).

SAMPLES AND METHODOLOGY

Chromite grains from Late Triassic-Early Jurassic Alaskan-type intrusions (Table 1) were analyzed at the Geological Survey of Canada (Ottawa, ON) during 2021-2023. Samples from dunitic portions of Tulameen, Polaris, Dortatelle Creek, Wrede Creek, Lunar Creek, and Turnagain Alaskan-type intrusions (Nixon et al., 1997, 2020a, 2020b; Nott et al., 2020; Ootes et al., 2020; Milidragovic et al., 2021) were selected from the existing collections at the Geological Survey of Canada and the British Columbia Geological Survey. New samples from the Wrede Creek and Lunar Creek intrusions were collected during the 2022 summer field season (Milidragovic and Cleven, 2023). All analyses were performed on polished sections (27 mm x 46 mm). Where possible, chromite grains from both

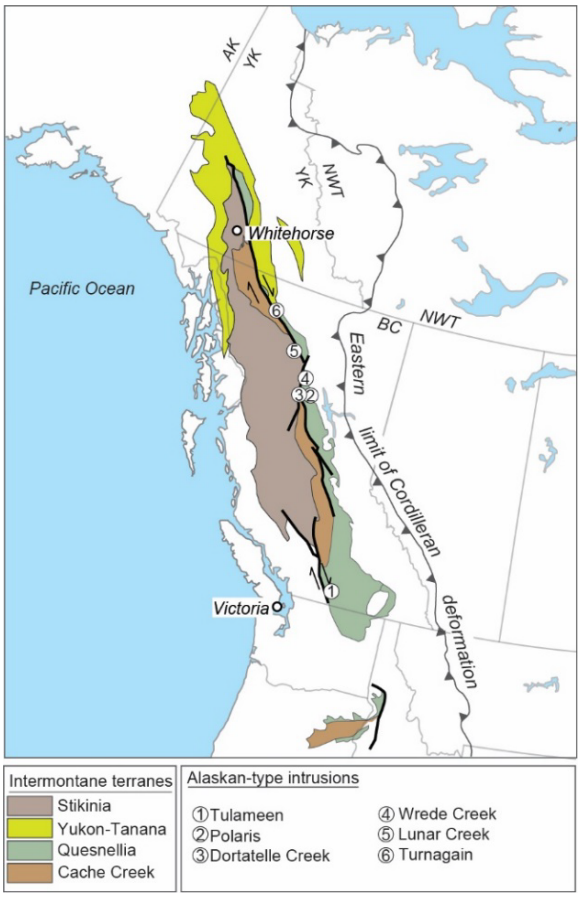

Figure 1. *Intermontane terranes of the northern Cordillera and locations of analyzed chromite samples.*

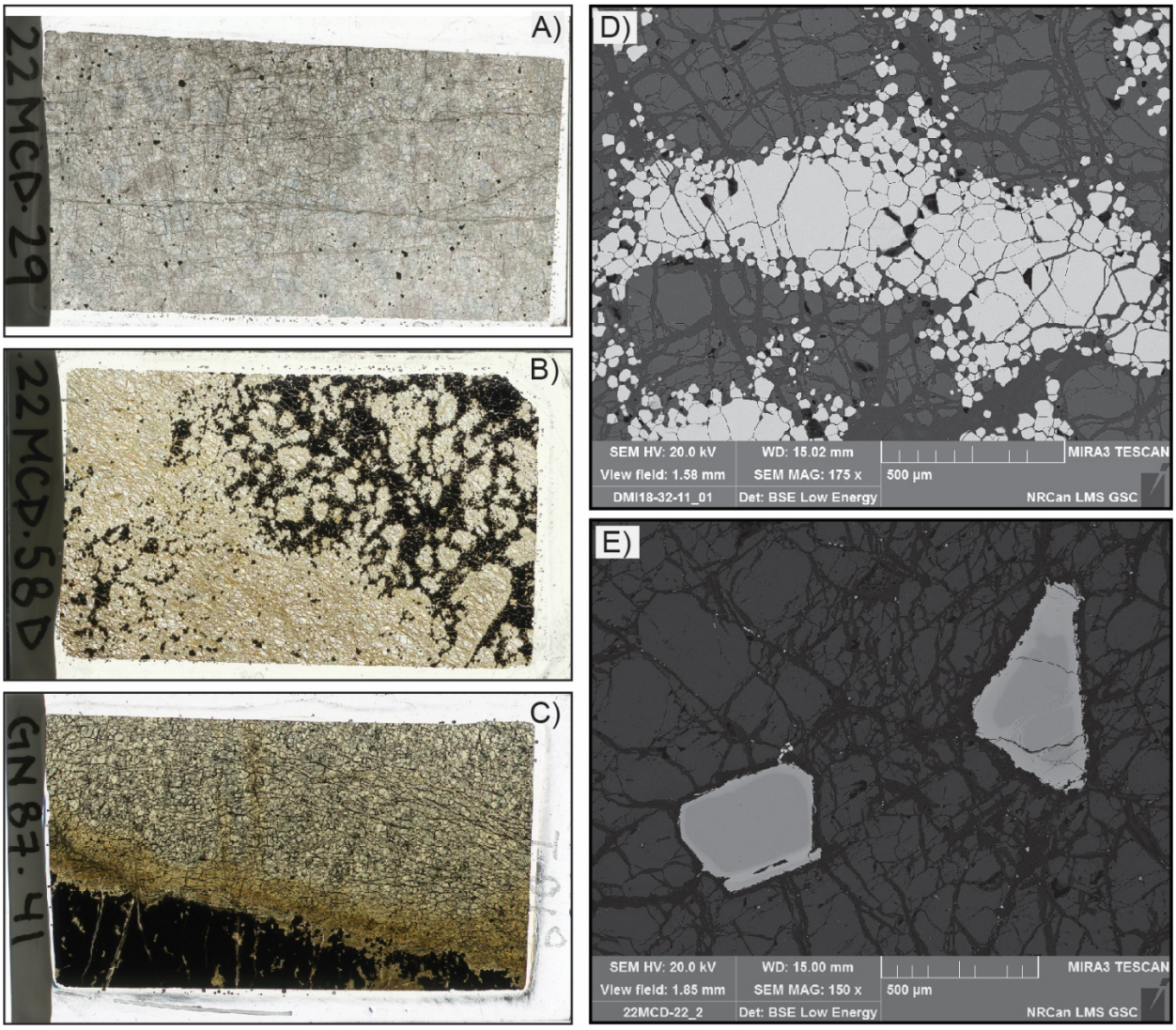

Figure 2. *Representative photomicrographs of polished sections in transmitted light* ***(A-C)*** *and scanning electron microscope backscattered (BSE-SEM) images of chromite* ***(D-E)*** *from Alaskan-type intrusions in British Columbia.* ***A)*** *Dunite (22MCD-29) from the Wrede Creek intrusion containing sparse, disseminated, euhedral to subhedral grains of chromite.* ***B)*** *Net-textured chromite-rich dunite (22MCD-58D) from the Lunar Creek intrusion. Fine-to coarse-grained, euhedral to subhedral chromite grains form an interstitial network between fractured, moderately serpentinized olivine grains.* ***C)*** *Dunite (GN87-41) from the Tulameen intrusion containing a massive chromite schlieren.* ***D)*** *Net-textured chromitite schlieren from a layered, chromite-rich dunite (DMI18-32-11) of the Polaris intrusion. Away from the contact with olivine (dark grey), chromite (light grey) shows coarsening and polygonization with development of ~120° interfacial angles, interpreted to reflect sub-solidus annealing (Eales and Reynolds, 1986).* ***E)*** *Initially euhedral to subhedral chromite (medium grey), mantled by magnetite-rich rims ("ferritchromit"; light grey), likely formed during low-temperature serpentinization of olivine (dark grey).*

chromite-rich (whole-rock Cr_2O_3 >10 wt. %, determined by X-ray fluorescence) and chromite-poor dunites (Fig. 2) were analyzed in order to evaluate the effects of near-solidus olivine-chromite re-equilibration on trace element systematics of chromite.

Prior to EPMA, all sections (Table 1) were carbon-coated and imaged using backscatter electron (BSE) mode on a Tescan MIRA Field Emission Scanning Electron Microscope (FEG-SEM) in order to identify: 1) chromite grains of sufficient size for LA-ICP-MS analysis; and 2) major element zonation in chromite (Fig. 2 and Appendix 1).

Following imaging, select chromite grains were analyzed for major (Al_2O_3, Cr_2O_3, FeO^{TOT}, and MgO) and trace (SiO_2, TiO_2, V_2O_3, CaO, MnO, NiO, Nb_2O_5, ZrO_2, and ZnO) oxides, using a JEOL JXA-8230 electron microprobe equipped with five wavelength-dispersive spectrometers with a take-off angle of 40 degrees. Operating conditions were 20 kV accelerating voltage, 20 nA probe current, and both focused beam (<1 μm) and 1 μm spot sizes. Counting times varied from 10-60 seconds on peak, and from 5-30 seconds on background positions. Standards used were a mixture of natural and synthetic, oxides, minerals and pure metals. Data reduction was accomplished with a ZAF matrix correction. Iron speciation was calculated using the procedure of Droop (1987). In total, results of 312 EPMA analyses on 21 samples are reported in Appendix 2 and data are presented in Figs. 3-6.

Trace element compositions of chromite were acquired by LA-ICP-MS at the Geological Survey of Canada (Ottawa), with a focus on quantifying low-level PGE contents. Analyses were undertaken during separate sessions in 2021 and 2023, following the analytical protocols of Lawley et al. (2020). Spot analyses were acquired using a Photon Machines Analyte 193 nm Excimer laser (with a HelEx cell) coupled to an Agilent 7700x quadrupole ICP-MS (2021) and an Applied Spectra RESOlution-SE laser (S155 cell) coupled to an Agilent 8900 triple quadrupole ICP-MS (2023).

Samples were analyzed using the following laser conditions: a 40-135 μm spot diameter (most spots 80 to 110 μm), a repetition rate of 10 Hz, and a fluence of 4.5-5 J/cm^2. Each analysis comprised 50 seconds of background measurement (gas blank), 60 seconds of ablation, and 40-50 seconds of washout. The ablation aerosol was transported out of the laser cell using ~ 1 L/min (2021 – Analyte G2) or 0.5 L/min of He (2023 – RESOlution-SE), and mixed with ~ 1 L/min Ar prior to entering the ICP-MS. For both analytical sessions, reaction cell technology was employed (utilizing 4 ml/min He) to reduce the effects of overwhelming mass interferences on the PGEs (Pagé et al., 2016; Smith et al., 2022; 2023), including metal-argides such as $^{61}Ni^{40}Ar$ on ^{101}Ru and $^{65}Cu^{40}Ar$ on ^{105}Pd.

A total of 29 (2021) and 32 (2023) masses were measured on the ICP-MS, including total mass sweep periods of 400 ms and 350 ms, respectively. Dwell times of 1-4 ms were used for most major and trace elements, whereas 20-40 ms was used for the PGEs. In order to assess potential mass interferences on the PGEs, multiple isotopes were measured where possible (Fig. 7), including ^{99}Ru, ^{101}Ru, ^{102}Ru, ^{105}Pd and ^{108}Pd (for both sessions) and ^{188}Os and ^{189}Os (2023 only). Concentrations, determined from different isotopes, are well-correlated and generally agree within 20% relative, except at low concentrations approaching detection limits. Average trace element abundances for each sample are reported in Table 4, and the complete dataset is provided in Appendix 4.

Calibration was achieved using analyses of the United States Geological Survey's synthetic glass reference material GSE-1G (Guillong et al., 2005) and synthetic pyrrhotite Po726 (Sylvester et al., 2005), developed as a reference material for analyses of gold and PGEs. Quantification of chromite spot analyses was achieved using Fe (determined by EPMA) as an internal standard. To assess the accuracy of LA-ICP-MS data,

Table 1. List of samples and basic compositional characteristics of chromite

Loc.	Sample	Intrusion	Lat.	Long.	Lithology	$Cr/(Cr+Al+Fe^{3+})$	$Cr/(Cr+Al)$	Fe^{3+}/Fe^{TOT}
1	GN87-35	Tulameen	49.5283	-120.9031	dunite	0.42-0.46	0.72-0.76	0.44-0.50
1	GN87-41	Tulameen	49.5369	-120.9000	Cr-dunite	0.62-0.67	0.80-0.83	0.40-0.44
2	DMI18-8-4	Polaris	56.4470	-125.5746	dunite	0.60-0.69	0.72-0.82	0.31-0.35
2	DMI18-17-3	Polaris	56.4592	-125.5707	dunite	0.64-0.78	0.70-0.78	0.02-0.26
2	DMI18-18-7	Polaris	56.4507	-125.5853	dunite	0.61-0.70	0.78-0.82	0.33-0.38
2	DMI18-32-11	Polaris	56.4859	-125.6184	Cr-dunite	0.66-0.78	0.74-0.84	0.26-0.29
2	DMI19-6-2	Polaris			Cr-dunite	0.75-0.78	0.84-0.86	0.24-0.28
3	DMI19-22-13	Dortatelle	56.3932	-126.0714	dunite	0.59-0.62	0.77-0.98	0.35-0.50
3	DMI19-22-14	Dortatelle	56.3922	-126.0705	dunite	0.57-0.59	0.76-0.86	0.38-0.44
4	22MCD-22	Wrede	56.6693	-126.1181	dunite	0.55-0.64	0.73-0.78	0.34-0.40
4	22MCD-26B	Wrede	56.6709	-126.1283	dunite	0.57-0.63	0.71-0.76	0.33-0.38
4	22MCD-27	Wrede	56.6737	-126.1269	dunite	0.61-0.66	0.74-0.77	0.29-0.35
4	22MCD-29	Wrede	56.6780	-126.1302	dunite	0.60-0.64	0.75-0.77	0.32-0.35
4	22MCD-48A	Wrede	56.6825	-126.1218	Cr-dunite	0.61-0.66	0.76-0.77	0.30-0.36
5	GN89-8096	Lunar	57.9137	-127.4523	dunite	0.44-0.51	0.72-0.97	0.40-0.47
5	GN89-9098	Lunar	57.9096	-127.4668	Cr-dunite	0.52-0.55	0.74-0.78	0.39-0.40
5	22MCD-58C	Lunar	57.9190	-127.4704	dunite	0.51-0.58	0.72-0.76	0.37-0.40
5	22MCD-58D	Lunar	57.9190	-127.4704	Cr- dunite	0.56-0.69	0.72-0.76	0.22-0.37
5	22MCD-60B	Lunar	57.9370	-127.4963	dunite	0.18-0.31	0.99-1.00	0.49-0.50
6	GN88-49	Turnagain	58.4857	-128.8492	Cr-dunite	0.78-0.83	0.86-0.89	0.23-0.30

Loc. – location as shown in Fig. 1; Lat. – latitude in decimal degrees; Long. – longitude in decimal degrees

samples of Stillwater chromite (provided by B. Kjarsgaard; Appendix 5), PTC-1b (nano-pressed powder pellet of certified nickel-copper sulfide concentrate by CanmetMINING – provided by D. Savard, Université du Québec à Chicoutimi) and NIST-612 were analyzed with the calibration standards following every twenty unknown analyses. Furthermore, sample DMI18-32-11 was included as a quality control sample during 2023 data collection, with the goal of assessing and developing it as an in-house chromite reference material.

In addition to performing LA-ICP-MS spot analyses, 2D element concentration maps were acquired with the goal of evaluating the extent of elemental heterogeneity and presence of mineral inclusions in chromite. Elemental maps were constructed using a series of laser line scans (8 µm @ 8 µm/s and 6 µm @ 12 µm/s; 60 Hz; 5 J/cm^2) following the method of Lawley et al. (2020). Raw signal intensities were converted to concentration profiles using line scans of GSE-1G and Po726 reference materials, including normalization of the total element oxides to 100 wt.%. Data were processed using LAMTRACE and PixeLAte spreadsheet programs (Jackson, 2008), with the concentration data converted to 2D element images using an in-house Python script.

RESULTS

Electron Probe Microanalysis

Major element compositions of chromite from all six intrusions show variable intrasample heterogeneity, with the most significant variation exhibited by the measured Cr_2O_3 and calculated FeO and Fe_2O_3 concentrations (Fig. 3, Appendix 3). The measured concentrations of SiO_2, CaO, Nb_2O_5, and ZrO_2 are typically at, or below, limits of detection (Appendix 3).

Figures 4 and 5 show the major element compositions of chromite from Alaskan-type intrusions reported herein compared to the empirical discriminant fields of Barnes and Roeder (2001) and Kamenetsky et al. (2001). Overall, in a given intrusion, chromite grains from chromite-rich samples have higher molar $Cr/(Cr+Al)$, $Cr/(Cr+Al+Fe^{3+})$, $Mg/(Mg+Fe^{2+})$, Fe^{3+}/Fe^{TOT} and lower molar $Fe^{3+}/(Cr+Al+Fe^{3+})$ than chromite from chromite-poor dunites. This is consistent with the greater extent of post-crystallization re-equilibration with olivine or trapped interstitial melt in chromite-poor dunites (Irvine, 1965; Barnes et al., 2022; Barnes et al., 2023). The purported trapped melt may be in part

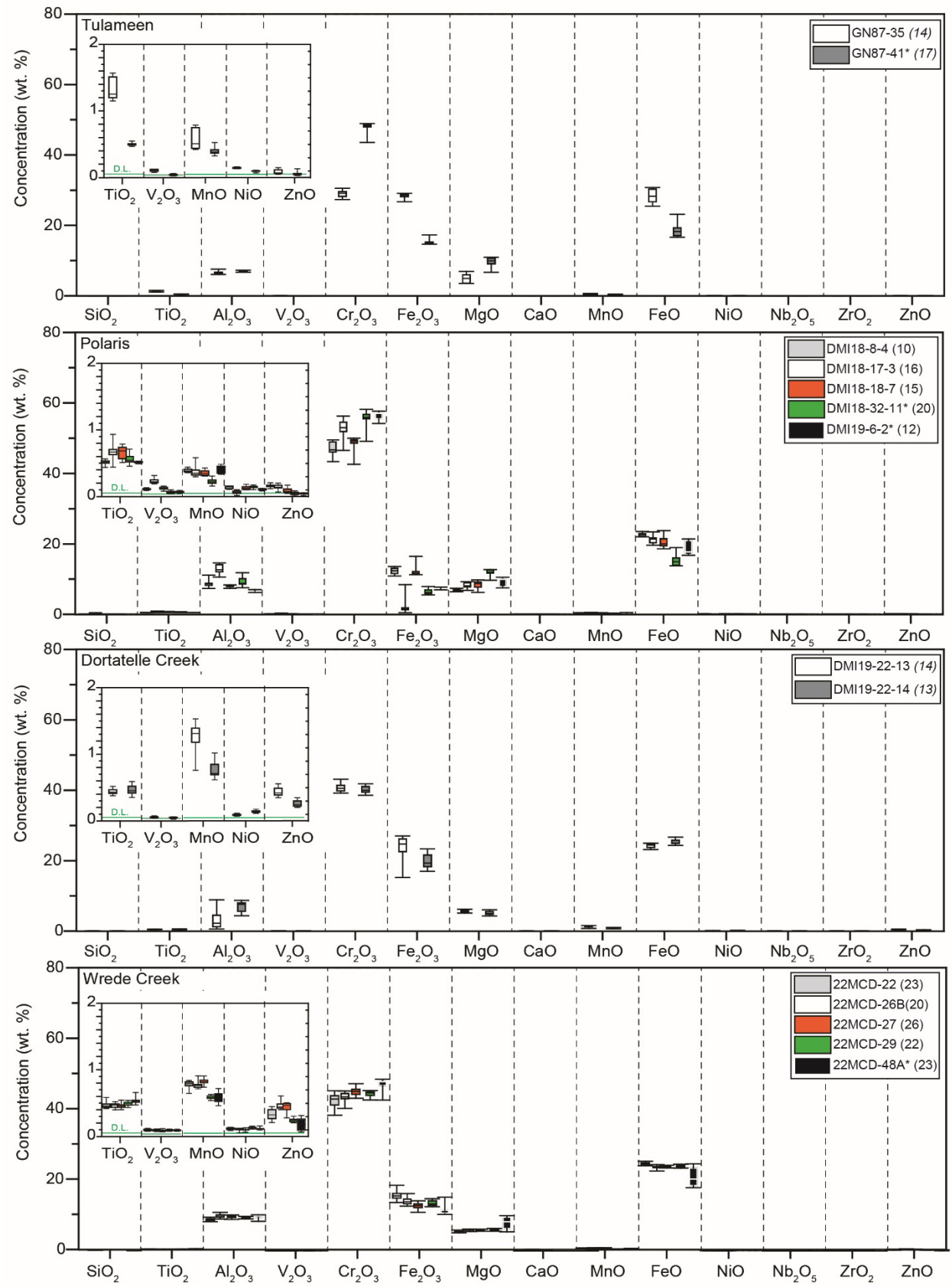
Tulameen
GN87-35 (14)
GN87-41* (17)
Polaris
DMI18-8-4 (10)
DMI18-17-3 (16)
DMI18-18-7 (15)
DMI18-32-11* (20)
DMI19-6-2* (12)
Dortatelle Creek
DMI19-22-13 (14)
DMI19-22-14 (13)
Wrede Creek
22MCD-22 (23)
22MCD-26B(20)
22MCD-27 (26)
22MCD-29 (22)
22MCD-48A* (23)
Concentration (wt. %)
D.L.
SiO2 TiO2 Al2O3 V2O3 Cr2O3 Fe2O3 MgO CaO MnO FeO NiO Nb2O5 ZrO2 ZnO
TiO2 V2O3 MnO NiO ZnO

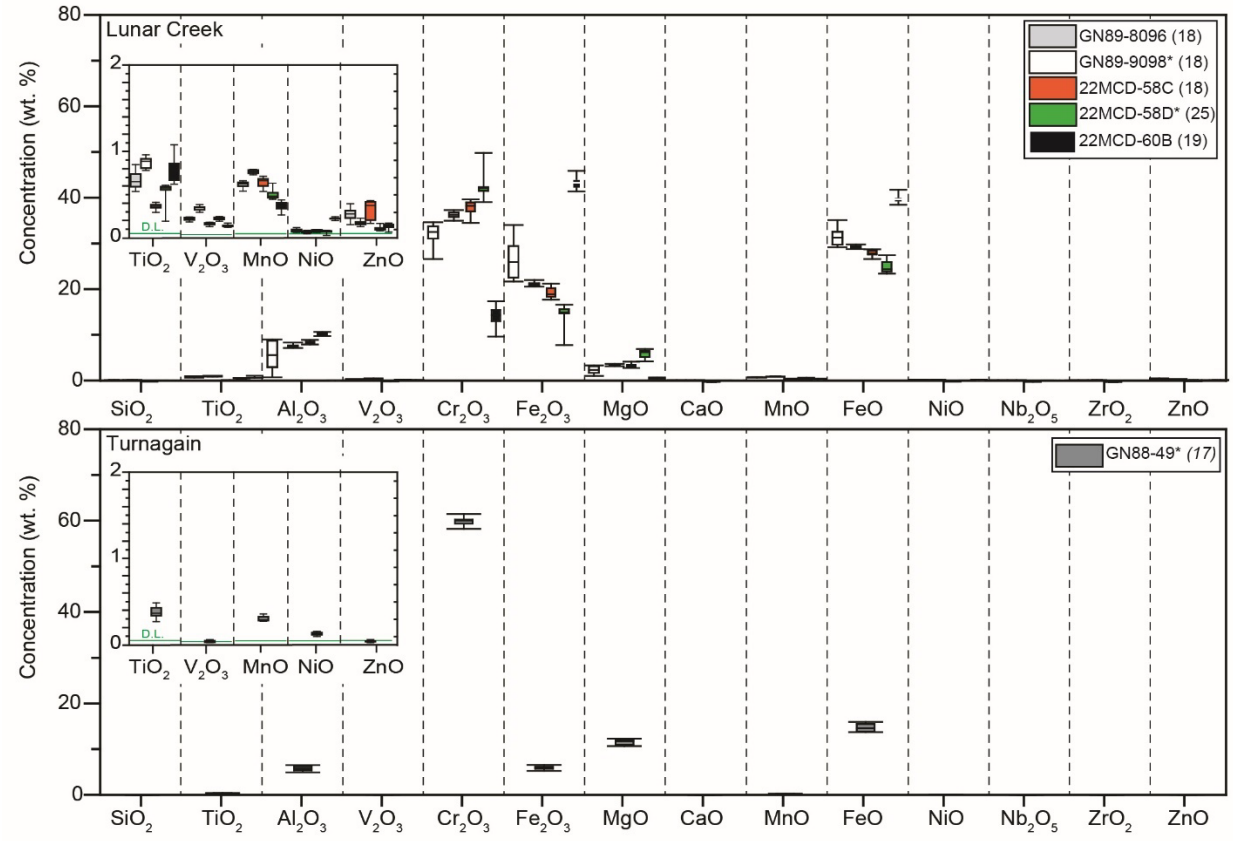

Figure 3. *Box-and-whisker (median, 25th and 75th percentile, 2.5th and 95th percentile) plots of electron probe microanalyses of chromite from Tulameen, Polaris, Dortatelle Creek, Wrede Creek, Lunar Creek, and Turnagain Alaskan-type intrusions. Inset shows minor element concentrations (note the change in the scale of the ordinate axis) and approximate detection limit (D.L.). Chromite-rich samples are denoted with "*" in the legend.*

represented by interstitial clinopyroxene, but may also have been expelled during compaction and or deformation. Chromite-poor dunites from several intrusions (Dortatelle Creek, Lunar Creek, and Turnagain) are depleted in Al_2O_3, as manifested by Cr/(Cr+Al) ratios that approach unity at Mg/(Mg+Fe^{2+}) <0.4, and elevated Fe^{3+}/(Cr+Al+Fe^{3+}) that can also approach unity. Such compositional trends are consistent with low-pressure metamorphic compositional changes (Barnes and Roeder, 2001) under relatively oxidizing conditions (i.e., not buffered by olivine hydration reactions that release H_2) observed in ophiolitic non-porous ferritchromites (Colás et al., 2014). Chromite-rich dunites from individual intrusions also display some notable differences in chromite compositions (Fig. 6). There is a progressive decrease in Cr/(Cr-Al) and Mg/(Mg+Fe^{2+}) and an increase in Fe^{3+}/(Cr+Al+Fe^{3+}) of Cr-spinel in Cr-rich rocks from Turnagain → Polaris → Tulameen → Wrede Creek →Lunar Creek. Although further study is needed to determine the role of the oxidation state on chromite compositions from different intrusions, these differences may signify differences in the level of incompatible element depletion (e.g., Al relative to Cr, Fe^{2+} relative to Mg) of magmas parental to each intrusion resulting from different extents of mantle melting (Fig. 5), with Turnagain and Polaris having the highest Cr/(Cr+Al) and Mg/(Mg+Fe^{2+}) and consequently trending towards the boninite field of the Barnes and Roeder (2001) Cr-spinel discrimination plot. In contrast, chromite grains from chromite-rich dunites of the Tulameen, Wrede Creek, and Lunar Creek intrusions plot

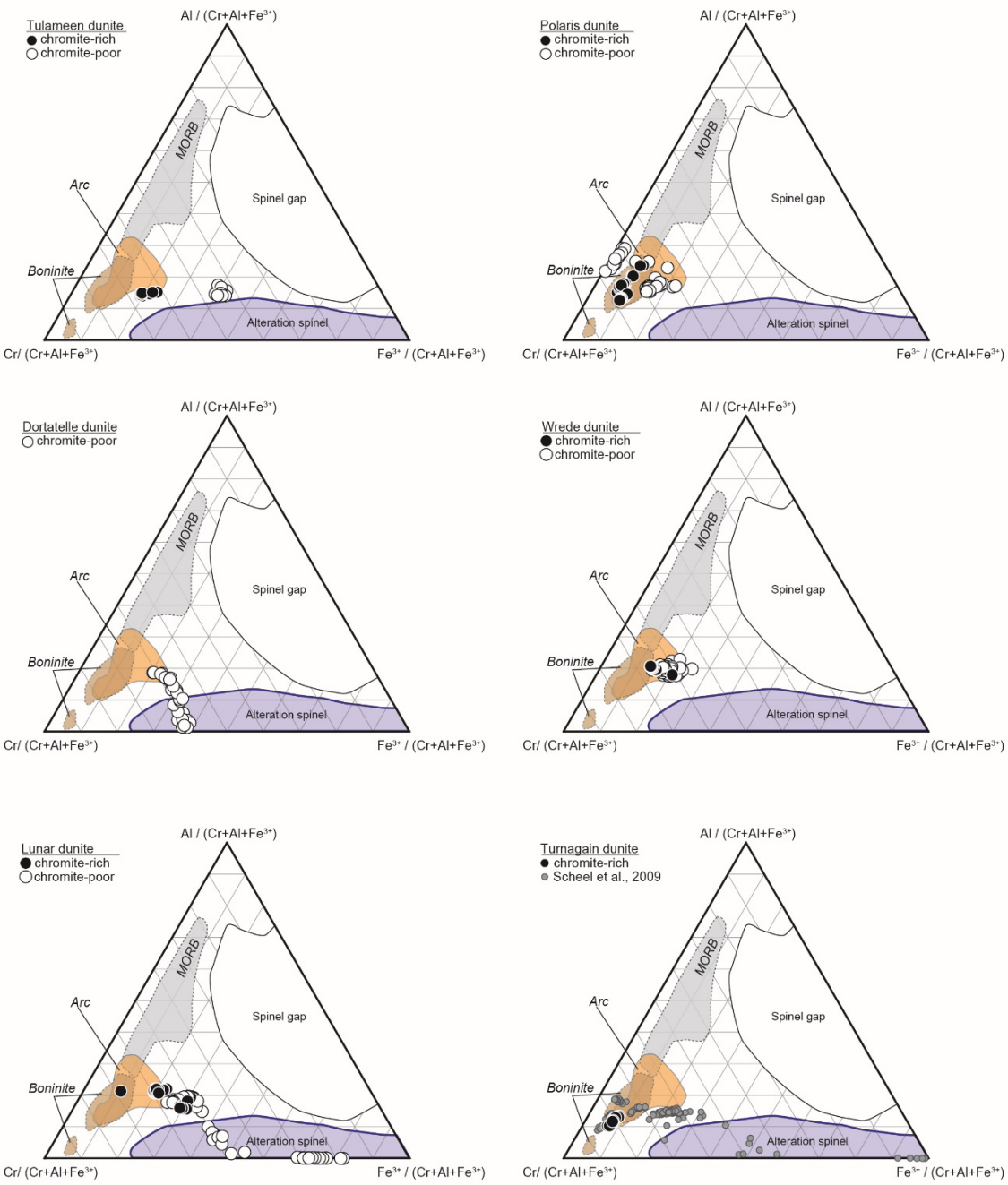

Figure 4. *Ternary diagrams of trivalent cations (Cr-Al-Fe^{3+}) showing chromite compositions from the Tulameen, Polaris, Dortatelle Creek, Wrede Creek, Lunar Creek, and Turnagain intrusions, compared to compositional fields for Cr-spinels from volcanic rocks of MORB, island arc, and boninite affinity. Compositional fields and the spinel gap are from Barnes and Roeder (2001). The spinel alteration field is from Hodel et al. (2020) and includes compositions of ferritchromit, Cr-magnetite, and magnetite. Chromites from chromite-poor dunites and Cr-rich dunites are distinguished. The plot of chromite from the Turnagain intrusion also includes the data from Scheel et al. (2009).*

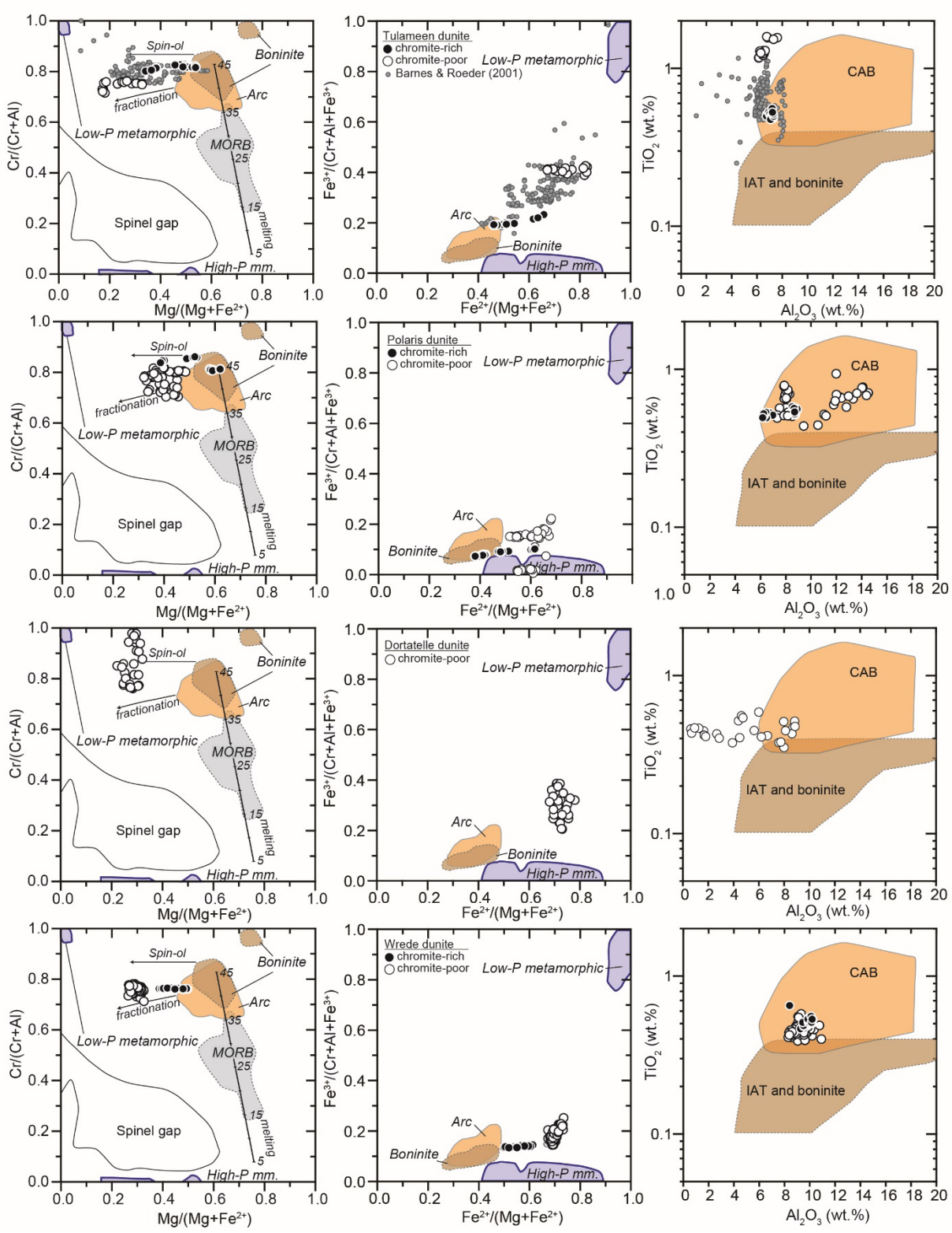
Spin-ol
Boninite
45
Arc
fractionation
35
Low-P metamorphic
MORB
25
15 melting
5
Spinel gap
High-P mm.
Cr/(Cr+Al)
Mg/(Mg+Fe2+)
Tulameen dunite
chromite-rich
chromite-poor
Barnes & Roeder (2001)
Low-P metamorphic
Arc
Boninite
High-P mm.
Fe3+/(Cr+Al+Fe3+)
Fe2+/(Mg+Fe2+)
CAB
IAT and boninite
TiO2 (wt.%)
Al2O3 (wt.%)
Polaris dunite
Dortatelle dunite
Wrede dunite

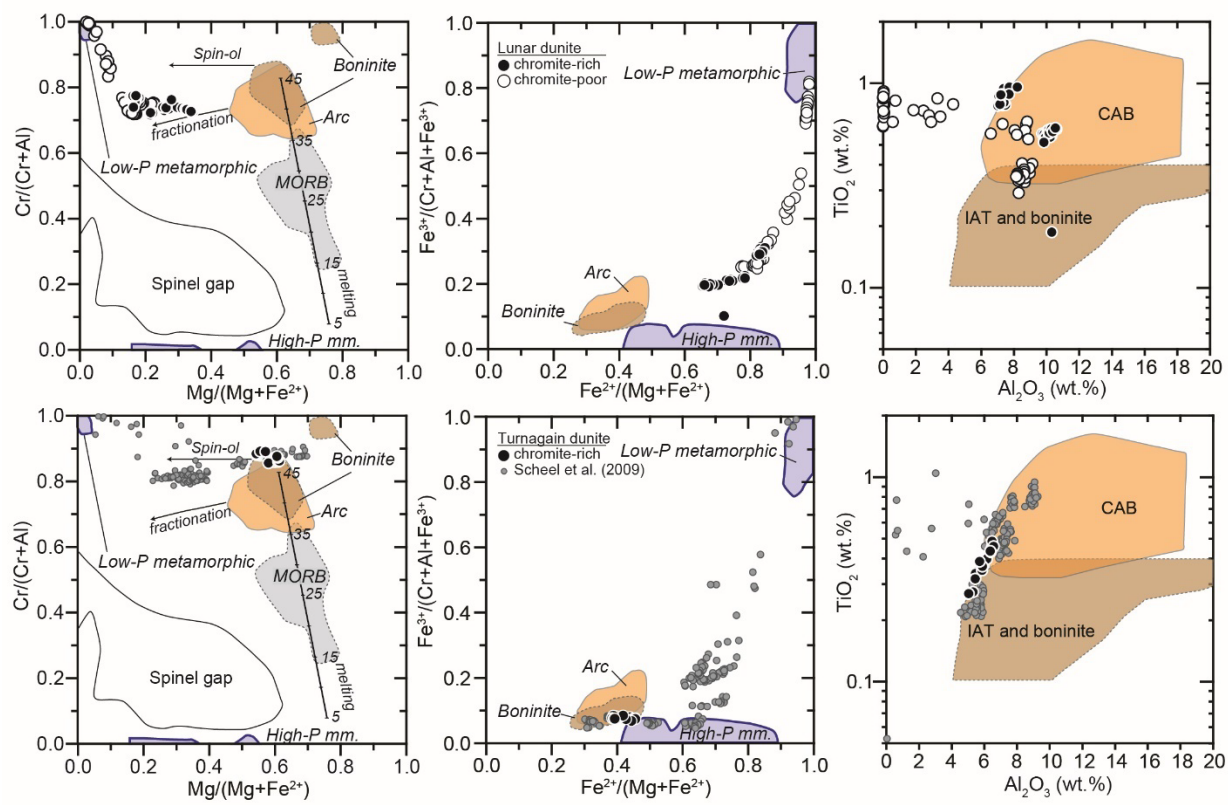

Figure 5. *Diagrams of molar Cr/(Cr+Al) vs. Mg/(Mg+Fe^{2+}) and Fe^{3+}/(Cr+Al+Fe^{3+}) vs. Fe^{2+}/(Mg+Fe^{2+}) and TiO_2 (wt.%) vs. Al_2O_3 (wt.%) showing chromite compositions from the Tulameen, Polaris, Dortatelle Creek, Wrede Creek, Lunar Creek, and Turnagain intrusions, compared to compositional fields for Cr-spinels from mafic volcanic rocks of calc-alkaline (CAB)and boninite/island arc tholeiite (IAT) affinity and metamorphic Cr-spinels. Compositional fields and the spinel gap for the two panels on the left side are from Barnes and Roeder (2001); compositional fields for the panels on the right are from Kamenetsky et al. (2001). The degree of partial melting scale and the fractionation trend for olivine$_{0.99}$:spinel$_{0.01}$ are from Pagé et al. (2008) and the compositional trend of subsolidus chromite re-equilibration with olivine is from Bédard and Hébert (1998). The plot of chromite from the Turnagain intrusion also includes the data from Scheel et al. (2009).*

solely within the island arc field of Barnes and Roeder (2001). Similarly, chromite from the Turnagain intrusion plots within the low-TiO_2 boninite/island arc tholeiite field of Kamenetsky et al. (2001), whereas chromites from other Alaskan-type intrusions do not show the same level of TiO_2 depletion and plot within the calc-alkaline basalt field. Notably, boninites are TiO_2-poor, MgO-rich lavas recognized for their abundance of orthopyroxene and elevated SiO_2 concentrations (Le Bas, 2000; Pearce and Reagan, 2019). They are not considered likely parental magmas to orthopyroxene-free Alaskan-type intrusions, likely warranting further refinement of spinel discrimination diagrams. The further need for refinement of spinel discrimination diagrams is also illustrated by chromite from the Polaris intrusions, which has boninitic affinities according to criteria of Barnes and Roeder (2001), but is decisively calc-alkaline basalt-like according to the criteria of Kamenetsky et al. (2001).

LA-ICP-MS analysis

Spatial heterogeneity

Previously acquired BSE images of chromite from the Polaris intrusion (Milidragovic et al.,

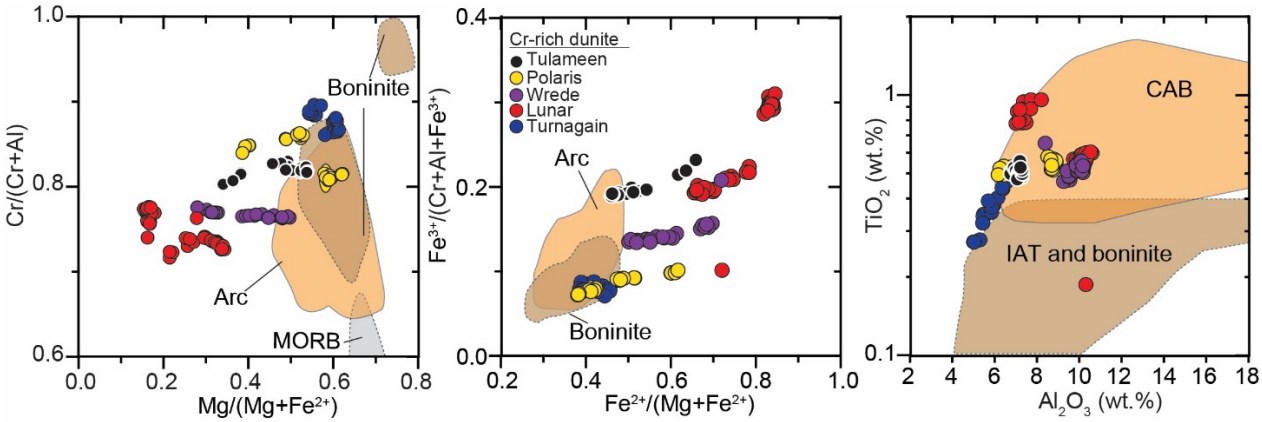

Figure 6. *Diagrams of molar Cr/(Cr+Al) vs. Mg/(Mg+Fe^{2+}), Fe^{3+}/(Cr+Al+Fe^{3+}) vs. Fe^{2+}/(Mg+Fe^{2+}), and TiO_2 (wt.%) vs. Al_2O_3 (wt.%) showing chromite compositions from chromite-rich dunites from Tulameen, Polaris, Wrede Creek, Lunar Creek, and Turnagain intrusions, compared to compositional fields for Cr-spinels from mafic volcanic rocks of calc-alkaline (CAB) and boninite/island arc tholeiite (IAT) affinity. Compositional fields and the spinel gap for the two panels on the left side are from Barnes and Roeder (2001); compositional fields for the panels on the right are from Kamenetsky et al. (2001).*

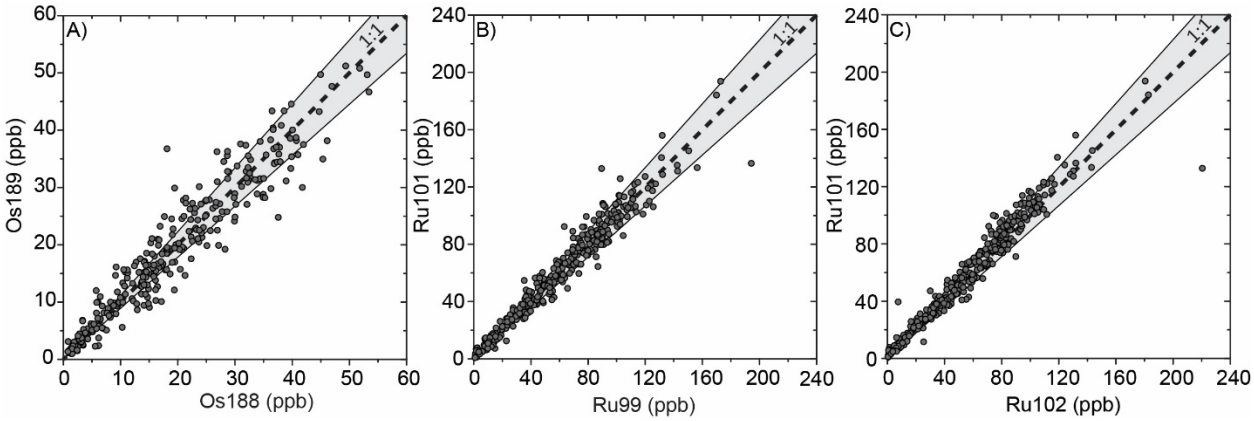

Figure 7. *LA-ICP-MS-determined concentrations of Os and Ir in chromite measured using multiple isotopes.* ***A)*** *Os (ppb) measured using ^{189}Os and ^{188}Os.* ***B)*** *Ru (ppb) measured using ^{101}Ru and ^{99}Ru.* ***C)*** *Ru (ppb) measured using ^{101}Ru and ^{102}Ru. The 10% relative deviation (grey field) around the 1:1 line (heavy dashed line) is shown for reference.*

2021) indicated the rare presence of micrometer-scale inclusions of laurite (RuS_2). Backscatter electron images acquired during this study (Appendix 1) indicate that chromite from the Lunar Creek intrusion hosts rare micrometer-scale inclusions of sperrylite ($PtAs_2$), a Pt-Ir-Rh-sulfide (e.g., bowieite), and a Pt-Fe alloy (Figs. 8A-C); chromite from the Polaris intrusion was also found intergrown with trace amounts of interstitial pentlandite (Fig. 8D), likely formed during serpentinization of olivine.

Elemental maps of two regions of massive chromite from Polaris sample DMI18-32-11 (Appendix 2), are unable to resolve these inclusions or the presence of geochemically distinct zones. The lone exception may be Cu-enriched zones in fine-grained chromite or along grain boundaries (Fig. 9). The absence of distinct

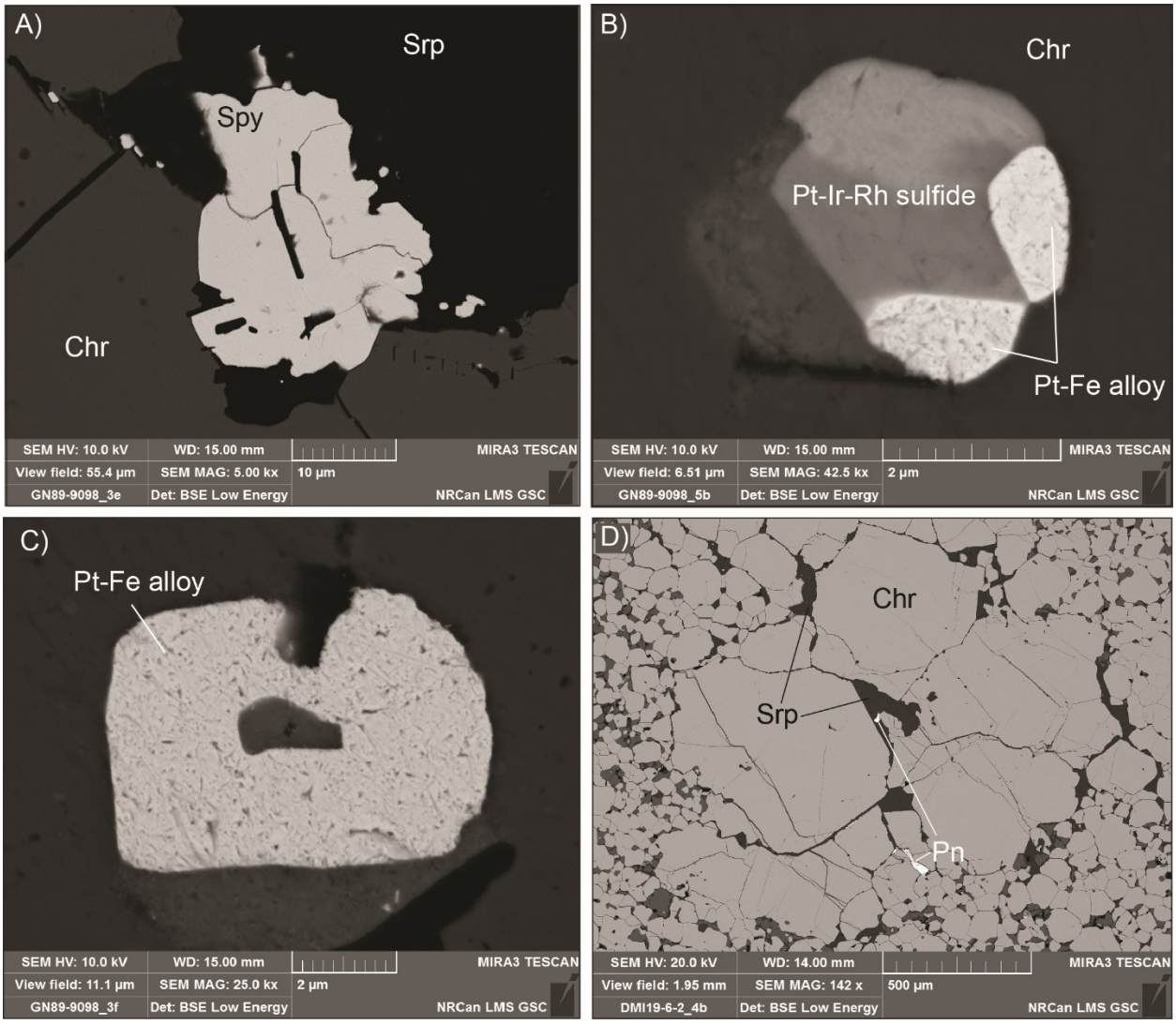

Figure 8. *BSE-SEM images of micrometer-scale platinum group mineral (PGM) inclusions* ***(A-C;*** *all from Lunar Creek sample GN89-9098****)*** *and interstitial sulfide* ***(D;*** *Polaris sample DMI19-6-2****)*** *hosted by chromite-rich dunites.* ***A)*** *Skeletal crystal of sperrylite at chromite-serpentine interface.* ***B)*** *Composite inclusion of Pt-Fe alloy and Pt-Ir-Rh sulfide in chromite.* ***C)*** *Monomineralic inclusion of Pt-Fe alloy in chromite.* ***D)*** *Interstitial pentlandite intergrown with chromite ±serpentine. Abbreviations: Chr- chromite, Pn – pentlandite, Spy – sperrylite, Srp – serpentine*

mineral inclusions may be due to the combined effect of very small inclusion size and the relatively high limits of detection (e.g., sub ppm levels compared to the ppb-level concentrations) imposed by the small ablation pit associated with the 6 µm beam diameter.

A closer look at the down-hole spectra of each analysis, however, indicates that nano- to micro-scale inclusions or heterogeneities (collectively referred to herein as inclusions) within chromite are ubiquitous in all intrusions except Dortatelle Creek (Table 2; Fig. 10). The most common types of mineral inclusions are rich in Cu without noticeable sulfur peaks. Complex inclusions enriched in Ir-Os-Ru ±(Rh-Cu) are also ubiquitous. Notably, Rh peaks are typically offset from or devoid of Cu signals, which suggests limited contribution of Cu-argide. Platinum-rich inclusions are uncommon and were only

Table 2. Summary of mineral inclusion/heterogeneity assemblages in chromite qualitatively identified by LA-ICP-MS

Sample	Intrusion	Inclusion-type
GN87-35	Tulameen	Rh-Ru ±Cu, Cu, Cu-sulfide
GN87-41	Tulameen	Cu
DMI18-8-4	Polaris	Ir ±Rh, Ir-Os-Ru ±Rh, Rh-Ru ±Ir, Cu, Ni-Cu-sulfide
DMI18-17-3	Polaris	Cu ±Ni
DMI18-18-7	Polaris	Ir-Os-Ru-Rh, Rh-Ru-Ir, Ru-sulfide, Cu, Ni-Cu-sulfide, Fe?-sulfide
DMI18-32-11	Polaris	Ru-Ir-Os ±Rh, Rh, Ru, Cu,
DMI19-6-2	Polaris	Ir-Os-Ru ±Rh, Ni, Cu
DMI19-22-13	Dortatelle	-
DMI19-22-14	Dortatelle	-
22MCD-22	Wrede	Cu
22MCD-26B	Wrede	Rh-Ru
22MCD-27	Wrede	Rh ±Ru ±Cu, Ir-Os, Cu
22MCD-29	Wrede	Rh-Ru ±Cu, Cu
22MCD-48A	Wrede	Rh, Cu
GN89-8096	Lunar	Ni-Cu (Rh-Ir-Os)-sulfide, Cu
GN89-9098	Lunar	Ir-Os-Ru-Rh-Pt-Cu, Rh, Cu
22MCD-58C	Lunar	Ir, Pt ±Rh, Rh-Ru ±Cu ±Ir ±Os, Cu ±Rh,
22MCD-58D	Lunar	Rh ±Ru ±Ir ±Os ±Pt ±Cu, Cu
22MCD-60B	Lunar	Rh-Ru-Ir, Rh-Pt-Ir, Cu
GN88-49	Turnagain	Ru ±Rh ±Ir ±Os, Cu

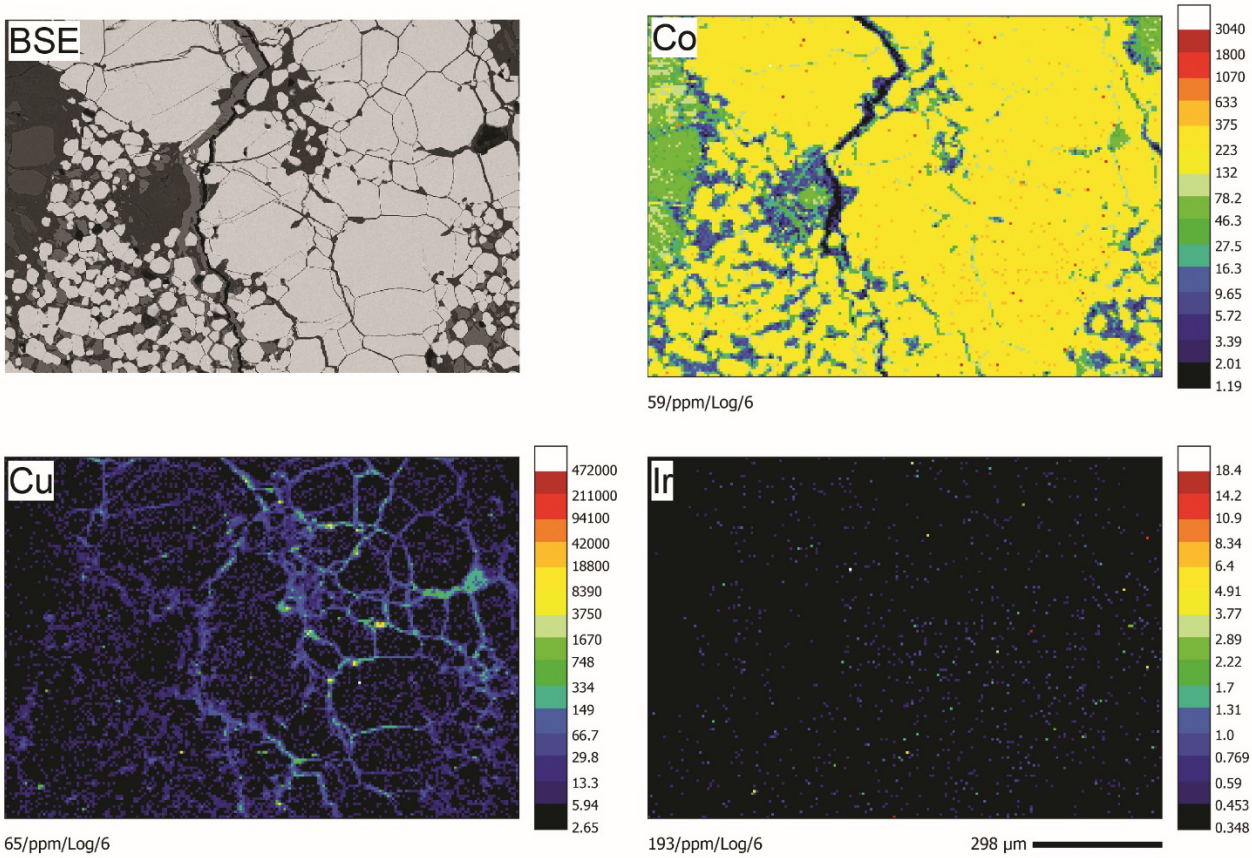

Figure 9. *BSE-SEM image of massive chromite from sample DMI18-32-11 and LA-ICP-MS elemental maps of Co, Cu and Ir of the same area. The maps were produced using laser line scans using a 6 µm diameter beam. Aside from Cu-enriched zones in fine-grained chromite and along grain boundaries, LA-ICP-MS mapping generally failed to identify compositional heterogeneity in chromite.*

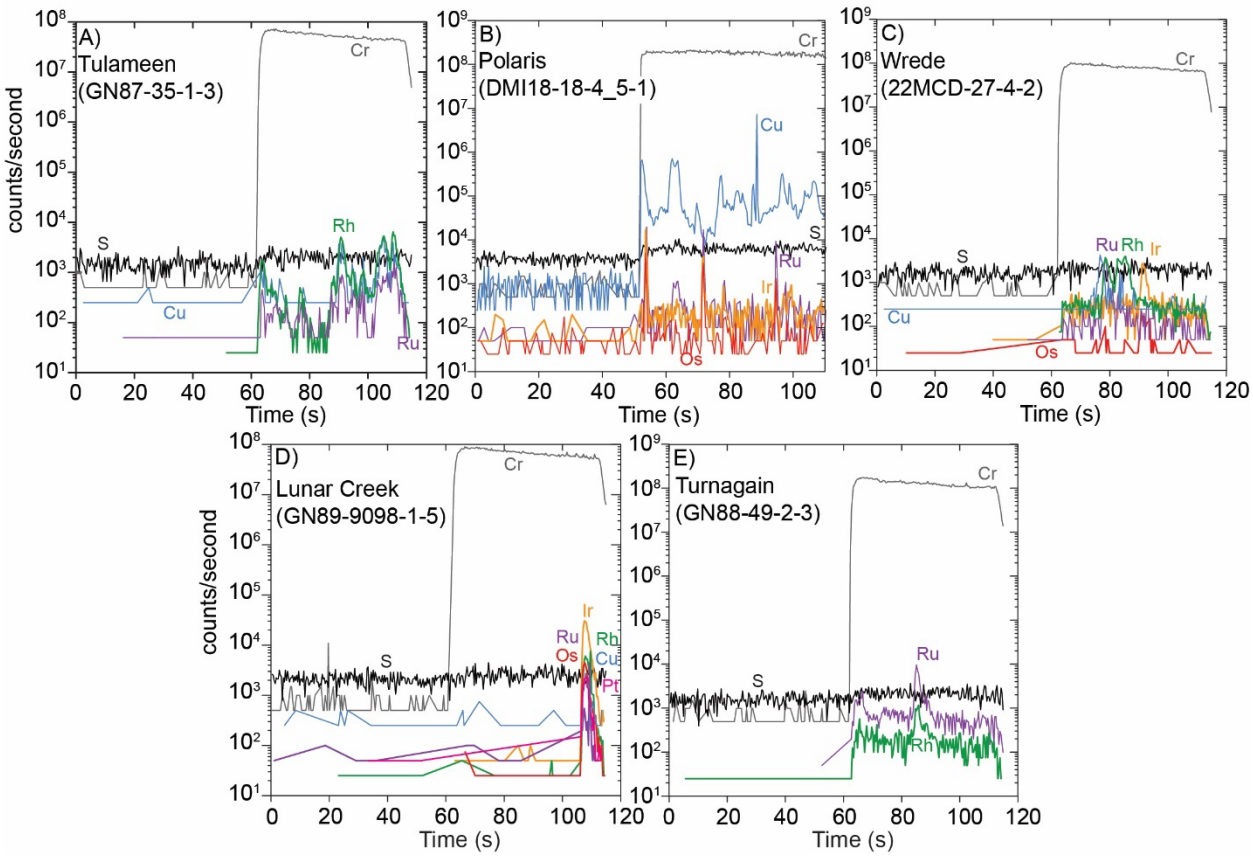

Figure 10. *Representative LA-ICP-MS time-resolved spectra through chromite grains from Alaskan-type intrusions in British Columbia.* ***A)*** *Rh-Ru-Cu- enriched heterogeneity/inclusion from Tulameen;* ***B)*** *Ir-Os-Ru- and Cu-enriched heterogeneites/inclusions from Polaris;* ***C)*** *Ir-Os, Rh ±Ru ±Cu enriched heterogeneities/inclusions from Wrede Creek;* ***D)*** *Ir-Os-Ru-Rh-Pt-Cu- enriched heterogeneity/inclusion from Lunar Creek;* ***E)*** *A Rh-Ru - enriched heterogeneity/inclusion from Turnagain.*

identified in chromites from the Lunar Creek intrusion. Surprisingly, no Pt-rich inclusions were identified in samples from the Tulameen intrusion, despite the intrusion's well-documented Pt-rich platinum-group metals (Nixon et al., 1990).

Detection limits and spot size

A key consideration prior to formal LA-ICP-MS analysis was determining the minimum spot diameter that would yield adequate detection and accuracy of PGEs, while minimally compromising the information on spatial heterogeneity of chromite grains. In 2021, using sample DMI18-32-11 which contains relatively coarse-grained chromite grains (Appendix 1), it was determined that concentrations of Re, Pt, Pd, Au were generally below the limits of detection (LOD) regardless of spot diameter, but spots ≥85 µm in diameter typically yield concentrations of Ir, Ru, Rh, ±Os above the LOD, with 135 µm spot size being preferred (Fig. 11A and B). Although the detection limits significantly improved in 2023 due to the use of a more sensitive ICP-MS, concentrations of Re, Pt, Au ± Pd were below detection; nonetheless it was determined that the detection limits associated with an 80 µm spot size were sufficiently low (e.g., <5 ppb) for determination of Ir, Os, Ru, and Rh concentrations at 10s to 100s of ppb (Fig. 11C and 10D).

Table 3. Average trace element concentrations in samples DMI18-32-11 and Stillwater that were used for quality control

	ppm									ppb						
	S^{34}	Sc^{45}	V^{51}	Co^{59}	Ni^{60}	Cu^{65}	Zn^{66}	Zr^{90}	Sn^{118}	Os^{189}	Ir^{193}	Ru^{101}	Rh^{103}	Pd^{105}	Pt^{195}	Au^{197}
Whole rock 32-11	**50**	**12.9**	**333**	**167**	**1189**	**9.2**	**220**	**<4**	**<0.17**	**12.1**	**17.7**	**47.2**	**9.94**	**0.55**	**2.22**	**0.8**
32-11 (2021; n = 21)	383	-	477	247	1071	5.0	316	0.32	0.16	-	20	18	6.3	-	-	-
RSD (%)	*17*	-	*10*	*13*	*5.9*	*66*	*18*	*19*	*5.5*	-	*30*	*59*	*86*	-	-	-
32-11 (2023; n = 23)	421	7.9	473	218	1227	12.9	322	0.25	0.19	14	20	36	2.8	0.68	-	-
RSD (%)	*17*	*2.2*	*1.0*	*1.2*	*2.3*	*28*	*3.9*	*25*	*7.6*	*197*	*52*	*148*	*64*	*18*	-	-
Mean 32-11*	**404**	**7.9**	**475**	**232**	**1154**	**9.2**	**319**	**0.29**	**0.17**	**14**	**19**	**28**	**4.1**	**0.68**	**-**	**-**
RSD (%)	*17*	*2.2*	*7.2*	*12*	*7.9*	*57*	*13*	*25*	*10.3*	*197*	*43*	*149*	*96*	*18*	-	-
Stillwater (2021; n =16)	477	-	1293	226	875	1.7	388	1.2	0.072	-	8.4	13	2.3	-	-	-
RSD (%)	*56*	-	*1.2*	*1.5*	*2.0*	*50*	*11*	*12*	*13*	-	*34*	*20*	*47*	-	-	-
Stillwater (2023; n =21)	604	5.7	1295	220	881	1.1	464	1.0	0.068	1.7	5.8	10.2	0.77	-	-	-
RSD (%)	*21*	*3.2*	*0.96*	*1.2*	*1.2*	*50*	*3.4*	*20*	*16*	*58*	*42*	*53*	*71*	-	-	-
Mean Stillwater*	**570**	5.7	**1294**	**223**	**878**	**1.4**	**431**	**1.1**	**0.070**	**1.7**	**6.9**	**11**	**1.3**	-	-	-
RSD (%)	*29*	*3.2*	*1.1*	*1.8*	*1.6*	*55*	*11*	*19*	*15*	*58*	*42*	*50*	*79*	-	-	-

* Aggregate mean concentration and RSD calculated from LA-CP-MS analyses from both 2021 and 2023.

The whole-rock trace element concentrations in sample DMI18-32-11 were determined by infrared absorption (IA; S), X-ray fluorescence (XRF; Co, Ni, V, Zn), ICP-MS (Sc, Cu, Zr, Sn), and NiS fire assay (PGE, Au) at Geoscience Laboratories.

Precision and Accuracy

Trace element concentrations in chromites from DMI18-32-11, determined in 2021 and 2023 (Table 3) are generally in good agreement (Fig. 11A and 11C); replication of the data between two sessions indicates that there was no bias introduced by using different instrument setups. The LA-ICP-MS chromite data from sample DMI18-32-11 closely match the whole-rock (WR) concentrations, including PGEs as determined by NiS fire assay, measured at the Ontario Geological Survey Geoscience Laboratories (Sudbury, ON). The trace element concentrations of the Stillwater sample are also comparable between the 2021 and 2023 datasets, with the exception of Os and Rh which were below detection in 2021. Overall, the Ni-Cu-PGE concentrations in the Stillwater chromite are similar to published Stillwater chromitite data reported by Pagé et al. (2016). Notably, both our analyses and those by Pagé et al. (2016) contrast strongly with the PGE-rich character of chromitites from the Ultramafic Series of the Stillwater Complex reported by Barnes et al. (2016).

Overall, the analytical precision, expressed as relative standard deviation ($RSD = \frac{standard\ deviation}{mean}\ x\ 100\%$), was better in 2023 for trace elements present at ppm concentration levels, both in sample DMI18-32-11 and the sample from Stillwater intrusion (Table 3). The high RSD% of elements present at sub-ppm levels likely reflects nano- to micro-scale inclusions as discussed above (Fig. 10); the presence of nano- to micro-scale nuggets rich in iridium-subgroup PGE (IPGE), in particular, accounts for the large spread in measured concentrations of Os-Ir-Ru-Rh (Fig. 11).

While we observe general agreement in the PGE concentrations between the WR and LA-ICP-MS datasets, quantifying the accuracy of the PGE analyses is difficult. First, whole rock analysis of the chromite schlieren from sample DMI18-32-11 contains 10.32 wt.% SiO_2 (normalized to 100% anhydrous basis),

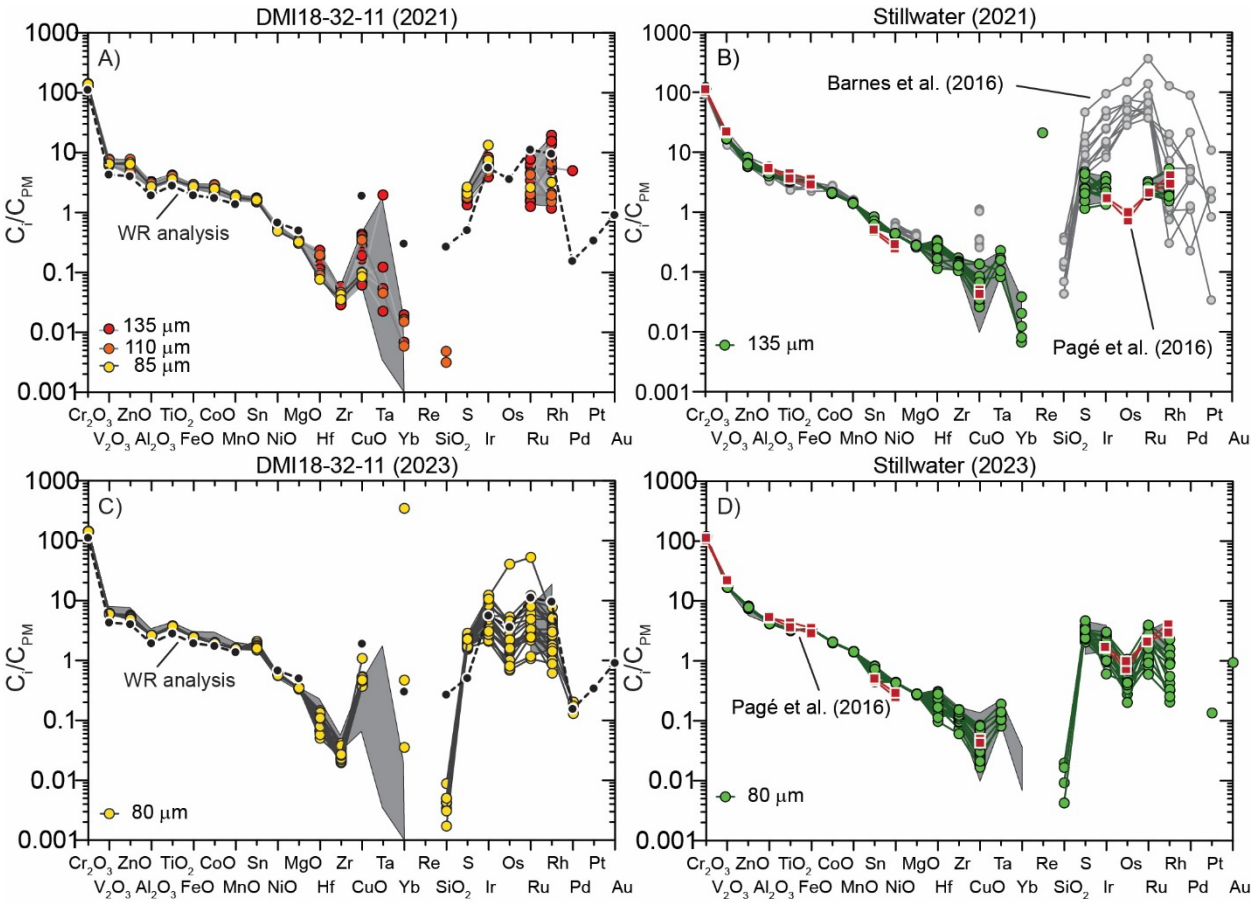

Figure 11. *Primitive mantle-normalized (Lyubetskaya and Korenaga, 2007) LA-ICP-MS trace element analyses of quality-control chromites analyzed in 2021 and 2023.* ***A)*** *Analyses of chromite from sample DMI18-32-11 analyzed with 85 µm, 110 µm, and 135 µm diameter laser beam size in 2021. Also shown are the whole-rock concentrations of trace elements in chromitite sample DMI18-32-11 (Geoscience Laboratories) as well as the 95th percentile confidence interval envelope for samples analyzed in 2021 (grey field);* ***B)*** *Analyses of Stillwater chromite from 2021 compared to LA-ICP-MS (Pagé et al., 2016) and whole-rock chromitite (SiO_2 <dl, Total oxide>90 wt.%; Barnes et al., 2016) analyses from the Stillwater complex. The 95th percentile confidence interval envelope for samples analyzed in 2021 is shown in grey;* ***C)*** *Analyses of chromite from sample DMI18-32-11 in 2023, compared to the 95th percentile confidence interval envelope for samples analyzed in 2021 and whole-rock concentrations* ***D)*** *Analyses of Stillwater chromite from 2023 compared to 95th percentile confidence interval envelope for samples analyzed in 2021 and LA-ICP-MS analyses of Pagé et al. (2016).*

of as much as ~25 wt.% serpentine in the sample, which could lead to discrepancies between the two datasets (e.g., Lawley et al., 2020). Secondly, varying sampling volumes between the two methods (i.e. bulk vs. micro-scale) and the documented presence of IPGE+Rh-rich heterogeneities in chromite, results in higher overall IPGE+Rh abundances measured by bulk rock dissolution methods than by in-situ analysis of chromite, consistent with earlier observations (Pagé et al., 2016).

Chromite trace element concentrations

The average trace element concentrations in chromites from Cordilleran Alaskan-type intrusions are listed in Table 4. The reported concentrations are averages of 10-20+ individual analyses. In the down-hole spectra, portions of

clean chromite were isolated from obvious Cu and platinum group mineral (PGM) inclusions. Select trace elements plotted against FeO^{TOT}, which we consider an index of combined differentiation, re-equilibration, and metamorphism, are shown in Figure 12. Primitive mantle-normalized (Palme and O'Neill, 2004; Lyubetskaya and Korenaga, 2007) concentrations of chalcophile (PGE + Au-Ni-Cu) elements are shown in Figure 13.

The chromites analyzed in this study show significant trace element variability that is underlain by two principal trends in trace element geochemical behaviour (Fig. 12). The causes and details of these different trends will be investigated in the future through comparison with other datasets (e.g., Barnes et al., 2023), but some key observations are given here. One trend, interpreted to reflect variable post-crystallization re-equilibration of chromite with olivine (±interstitial melt), shows a broadly linear increase in concentrations of divalent elements (Mn, Zn, Co; Fig. 12A-C) with increasing FeO^{TOT}, while the other trend, consistent with low-P metamorphism under relatively oxidizing conditions, shows a negative correlation between divalent element concentrations and FeO^{TOT} at FeO^{TOT} >44 wt.%. These two trends are not as evident in plots of more highly charged elements (Fig. 12D-F), which Barnes et al. (2023) consider to be immobile in rocks with >40 modal % chromite. Although Sc (+3), displays a general positive correlation with FeO^{TOT}, individual samples may also display nearly vertical trends when plotted against FeO^{TOT}, suggesting Sc was relatively mobile even in some Cr-rich samples from Lunar Creek.

Table 4. Average trace element concentrations in chromites from select Alaskan-type intrusions

	ppm									ppb				
	S^{34}	Sc^{45}	V^{51}	Co^{59}	Ni^{60}	Cu^{65}	Zn^{66}	Zr^{90}	Sn^{118}	Os^{189}	Ir^{193}	Ru^{101}	Rh^{103}	ΣIPGE+Rh
Tulameen														
GN87-35 (n = 14)	**343**	**10**	**694**	**315**	**1167**	**44**	**792**	**0.17**	**0.55**	**14**	**10**	**51**	**38**	**114**
RSD (%)	*31*	*37*	*9*	*26*	*3*	*356*	*43*	*79*	*16*	*27*	*43*	*37*	*94*	*47*
GN87-41 (n = 17)	**309**	**10**	**288**	**292**	**768**	**-**	**675**	**0.64**	**0.22**	**26**	**38**	**82**	**125**	**271**
RSD (%)	*18*	*6*	*2*	*22*	*3*	*-*	*52*	*23*	*12*	*23*	*53*	*7*	*14*	*11*
Polaris														
DMI18-8-4 (n = 11)	**461**	**-**	**729**	**379**	**1033**	**22**	**1188**	**0.36**	**0.08**	**28**	**33**	**70**	**30**	**157**
RSD (%)	*18*	*-*	*23*	*21*	*21*	*154*	*28*	*84*	*17*	*77*	*36*	*47*	*26*	*41*
DMI18-17-3 (n = 12)	**472**	**-**	**1339**	**367**	**418**	**10**	**1259**	**0.43**	**0.05**	**20**	**31**	**66**	**22**	**108**
RSD (%)	*32*	*-*	*15*	*10*	*14*	*212*	*35*	*79*	*92*	*11*	*63*	*41*	*54*	*66*
DMI18-18-7 (n = 11)	**298**	**-**	**848**	**295**	**999**	**1.8**	**633**	**0.31**	**0.09**	**29**	**37**	**79**	**37**	**172**
RSD (%)	*16*	*-*	*9*	*6*	*8*	*226*	*13*	*15*	*14*	*142*	*52*	*99*	*19*	*79*
DMI18-32-11 (n = 44)	**404**	**7.9**	**475**	**232**	**1154**	**9.2**	**319**	**0.29**	**0.17**	**14**	**19**	**28**	**4.1**	**58**
RSD (%)	*17*	*2.2*	*7.2*	*12*	*7.9*	*57*	*13*	*25*	*10.3*	*197*	*43*	*149*	*96*	*118*
DMI19-6-2 (n = 12)	**333**	**9.4**	**422**	**269**	**795**	**3.1**	**400**	**0.51**	**0.17**	**3**	**12**	**15**	**5**	**32**
RSD (%)	*15*	*13*	*2*	*20*	*15*	*79*	*18*	*29*	*4*	*50*	*52*	*81*	*97*	*45*
Dortatelle Ck.														
DMI19-22-13 (n = 18)	**256**	**1.4**	**362**	**400**	**685**	**-**	**3884**	**0.00**	**2.3**	**21**	**116**	**93**	**122**	**351**
RSD (%)	*19*	*38*	*9*	*17*	*10*	*-*	*19*	*89*	*50*	*16*	*16*	*13*	*8*	*1*
DMI19-22-14 (n = 14)	**292**	**5.1**	**303**	**472**	**1052**	**-**	**2318**	**0.01**	**0.23**	**31**	**129**	**105**	**114**	**379**

RSD (%)	*13*	*26*	*7*	*6*	*10*	*-*	*20*	*69*	*33*	*13*	*9*	*17*	*17*	*11*
Wrede Creek														
22MCD-22 (n =23)	**354**	**11**	**560**	**479**	**820**	**0.10**	**3074**	**0.07**	**0.10**	**26**	**22**	**55**	**41**	**144**
RSD (%)	*20*	*24*	*10*	*4*	*7*	*58*	*21*	*39*	*16*	*24*	*17*	*31*	*40*	*26*
22MCD-26B (n =20)	**398**	**9.8**	**551**	**296**	**757**	**0.06**	**4155**	**0.05**	**0.18**	**22**	**72**	**82**	**92**	**268**
RSD (%)	*20*	*20*	*5*	*4*	*18*	*28*	*8*	*61*	*83*	*15*	*14*	*23*	*21*	*16*
22MCD-27 (n =25)	**439**	**8.8**	**515**	**401**	**701**	**0.14**	**4050**	**0.07**	**0.11**	**14**	**76**	**76**	**68**	**234**
RSD (%)	*16*	*20*	*7*	*3*	*13*	*142*	*18*	*32*	*13*	*18*	*11*	*22*	*16*	*12*
22MCD-29 (n =22)	**395**	**11**	**538**	**507**	**985**	**0.16**	**2228**	**0.04**	**0.13**	**9.5**	**97**	**99**	**77**	**282**
RSD (%)	*17*	*13*	*3*	*6*	*6*	*93*	*10*	*34*	*14*	*24*	*11*	*17*	*24*	*15*
22MCD-48A (n =23)	**381**	**11**	**519**	**281**	**821**	**0.35**	**1554**	**0.37**	**0.13**	**34**	**58**	**99**	**102**	**293**
RSD (%)	*19*	*4*	*2*	*14*	*6*	*74*	*53*	*35*	*8*	*14*	*29*	*11*	*11*	*9*
Lunar Creek														
GN89-8096 (n =17)	**402**	**16**	**1397**	**368**	**593**	**-**	**2392**	**0.04**	**0.07**	**1.9**	**1.0**	**2.2**	**1.0**	**4.3**
RSD (%)	*36*	*15*	*7*	*9*	*13*	*-*	*22*	*28*	*14*	*43*	*55*	*55*	*74*	*52*
GN89-9098 (n =18)	**377**	**14**	**2160**	**368**	**520**	**0.26**	**1571**	**0.11**	**0.14**	**3.6**	**2.9**	**6.7**	**2.7**	**14**
RSD (%)	*19*	*15*	*6*	*8*	*6*	*156*	*13*	*70*	*16*	*89*	*112*	*41*	*248*	*80*
22MCD-58C (n =18)	**479**	**17**	**1025**	**430**	**605**	**1.04**	**2665**	**0.07**	**0.06**	**19**	**11**	**68**	**26**	**103**
RSD (%)	*26*	*8*	*4*	*8*	*5*	*172*	*35*	*47*	*27*	*122*	*125*	*138*	*187*	*145*
22MCD-58D (n =24)	**394**	**13**	**1370**	**320**	**529**	**0.75**	**920**	**0.22**	**0.08**	**17**	**18**	**49**	**76**	**160**
RSD (%)	*14*	*6*	*5*	*12*	*5*	*151*	*19*	*33*	*12*	*54*	*45*	*94*	*96*	*79*
22MCD-60B (n =19)	**285**	**7.1**	**854**	**220**	**1774**	**-**	**1005**	**0.13**	**0.13**	**1.3**	**3.7**	**2.5**	**6.5**	**8.0**
RSD (%)	*14*	*40*	*7*	*12*	*2*	*-*	*26*	*123*	*12*	*36*	*108*	*83*	*237*	*193*
Turnagain														
GN88-49 (n =20)	**330**	**5.6**	**280**	**269**	**1013**	**2.1**	**381**	**0.37**	**0.08**	**41**	**62**	**333**	**29**	**464**
RSD (%)	*15*	*7*	*22*	*14*	*11*	*144*	*6*	*18*	*14*	*17*	*10*	*32*	*18*	*23*

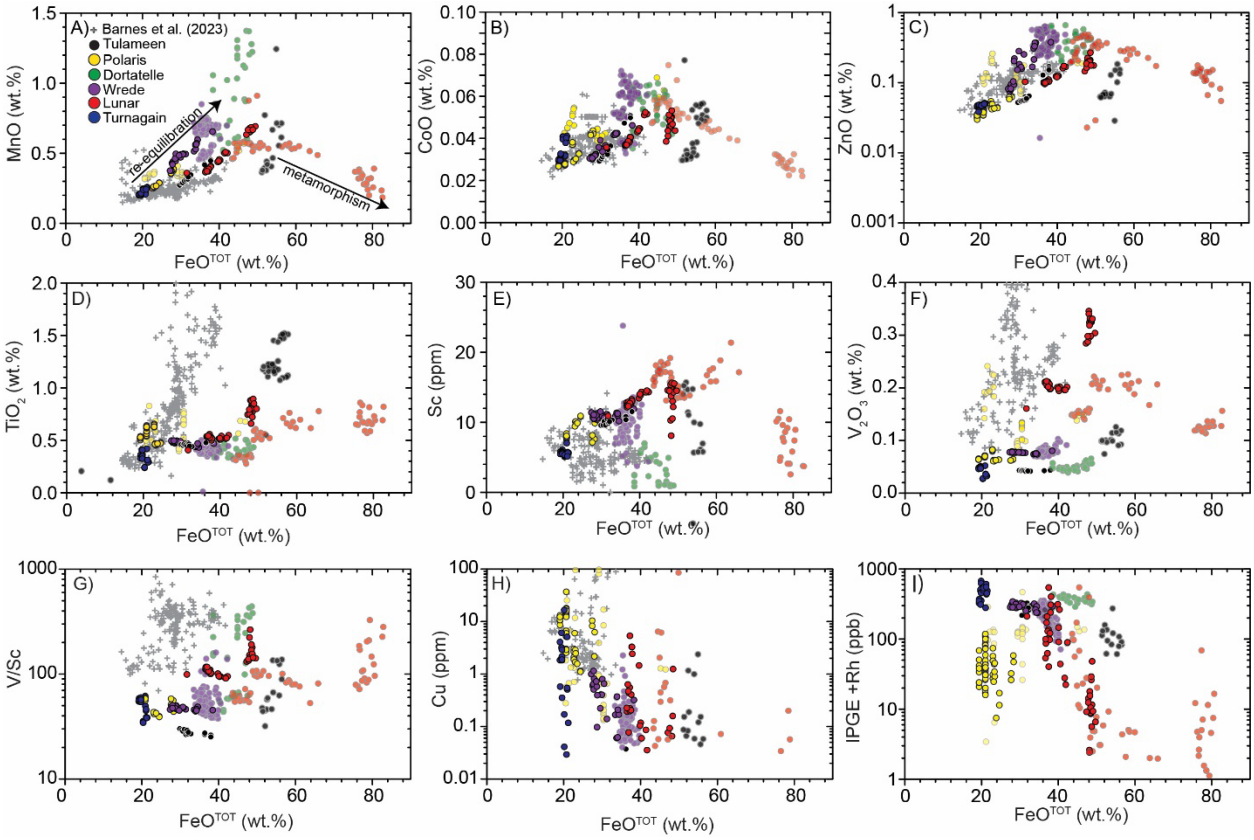

Figure 12. *Trace element concentrations plotted against FeO^{TOT} (wt.%). **A)** MnO (wt.%); **B)** CoO (wt.%); **C)** ZnO (wt.%); **D)** TiO_2 (wt.%); **E)** Sc (ppm); **F)* V_2O_3 *(wt. %); **G)** V/Sc; **H)** Cu (ppm); **I)** Total IPGE + Rh (ppb). Bold symbols indicate chromites from Cr-rich samples (Cr_2O_3 >10 wt. %), whereas chromites from Cr-poor samples (Cr_2O_3 <10 wt. %), which are more susceptible to post-crystallization re-equilibration, are indicated by faint symbols. Chromite analyses from Alaskan-type intrusions are compared to chromite compositions from within-plate komatiites, picrites, and layered intrusions (grey crosses; Barnes et al., 2023).*

With the exception of the same sample from Lunar Creek, Ti (+4) and V (+3 to +5 in terrestrial magmas) show a limited range of concentrations across a broad range of chromite FeO^{TOT}. Notably, chromite grains from the Lunar Creek intrusion are distinctly enriched in V_2O_3 (>0.2 wt.%) relative to the other intrusions (Fig. 12). Assuming relatively uniform V_2O_3 contents of Alaskan-type intrusion parental magmas, this may reflect a relatively reduced, low $f(O_2)$ Lunar Creek magma, given the negative dependence of $D_V^{chr\text{-}melt}$ on $f(O_2)$ (Lee et al., 2005).

Finally, clean (inclusion-free) Cu and PGE concentrations in chromite show large variability (Fig. 13), both across and within individual suites, that is independent of FeO^{TOT} (Fig. 12). Chromite grains from Dortatelle Creek, Wrede Creek, and Turnagain suites have relatively high PGE abundances that exceed those in plutonic rocks reported by Pagé et al. (2016), and generally fall within the empirically defined field of volcanic chromites.

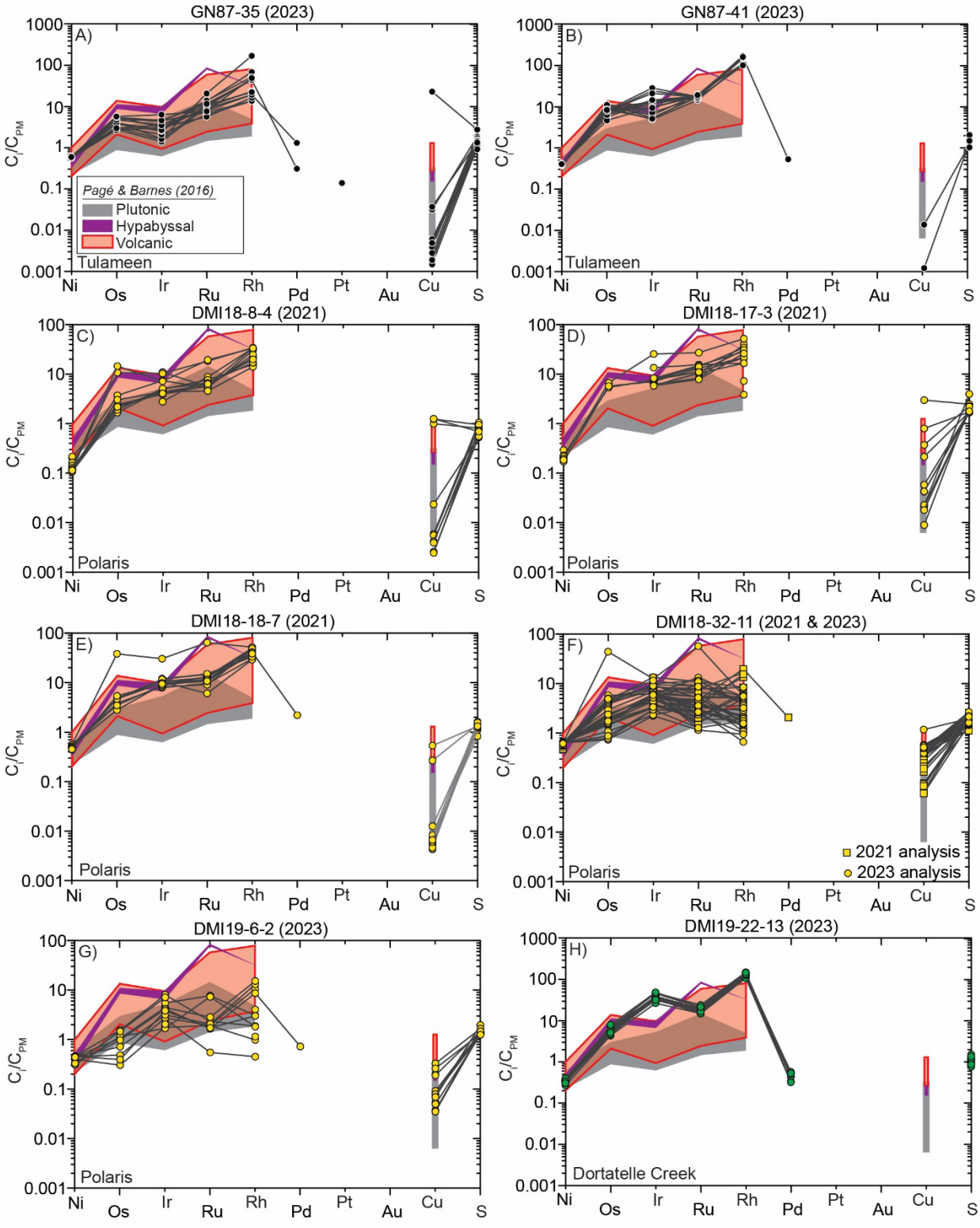
GN87-35 (2023)
A)
Pagé & Barnes (2016)
Plutonic
Hypabyssal
Volcanic
Tulameen
GN87-41 (2023)
B)
Tulameen
DMI18-8-4 (2021)
C)
Polaris
DMI18-17-3 (2021)
D)
Polaris
DMI18-18-7 (2021)
E)
Polaris
DMI18-32-11 (2021 & 2023)
F)
Polaris
2021 analysis
2023 analysis
DMI19-6-2 (2023)
G)
Polaris
DMI19-22-13 (2023)
H)
Dortatelle Creek
C_i/C_PM
Ni Os Ir Ru Rh Pd Pt Au Cu S

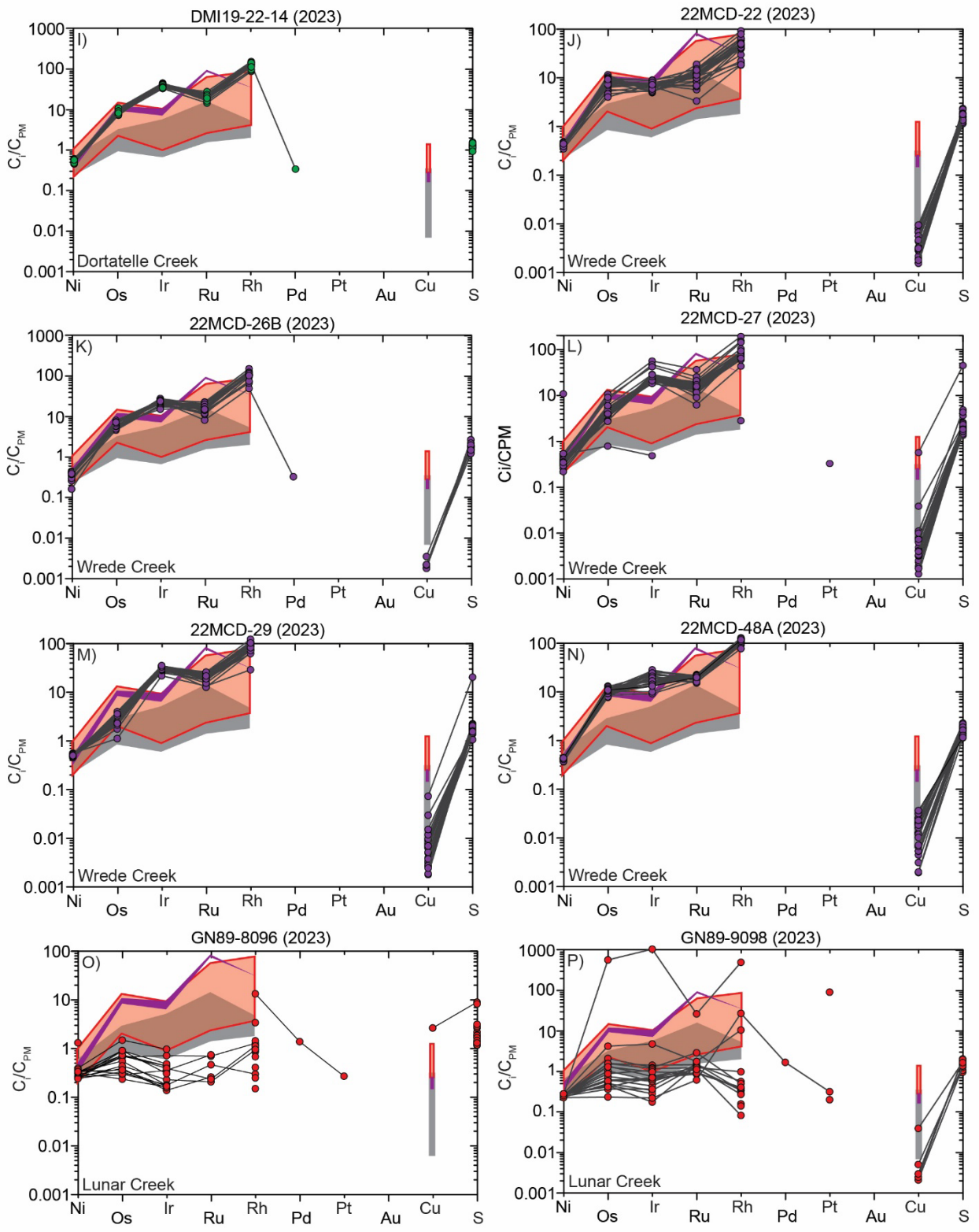
DMI19-22-14 (2023)
I)
Dortatelle Creek
22MCD-22 (2023)
J)
Wrede Creek
22MCD-26B (2023)
K)
Wrede Creek
22MCD-27 (2023)
L)
Wrede Creek
22MCD-29 (2023)
M)
Wrede Creek
22MCD-48A (2023)
N)
Wrede Creek
GN89-8096 (2023)
O)
Lunar Creek
GN89-9098 (2023)
P)
Lunar Creek
Ci/CPM
Ni Os Ir Ru Rh Pd Pt Au Cu S

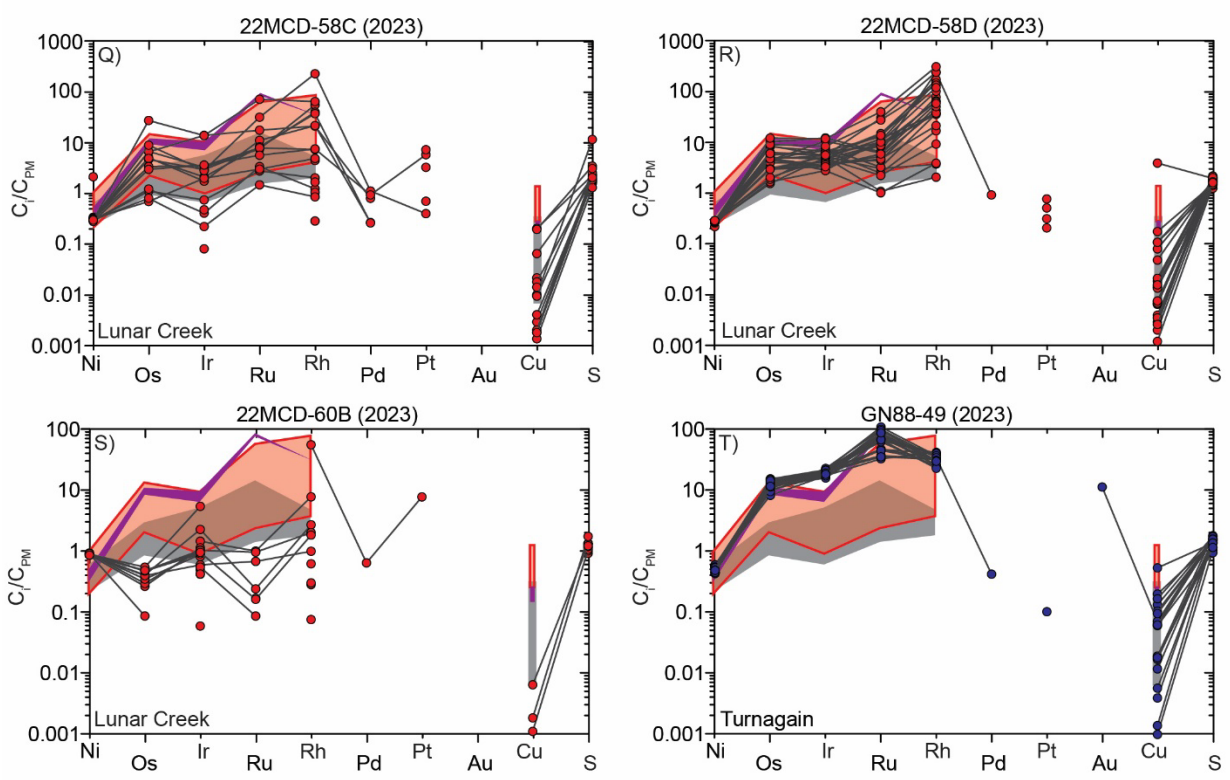

Figure 13. *Primitive mantle-normalized (Lyubetskaya and Korenaga, 2007) concentrations of chalcophile elements and S measured in individual chromite grains and plotted by sample.* ***A-B)*** *Tulameen;* ***C-G)*** *Polaris;* ***H-I)*** *Dortatelle Creek;* ***J-N)*** *Wrede Creek;* ***O-S)*** *Lunar Creek;* ***T)*** *Turnagain. Shown for reference are the compositions of volcanic, hypabyssal, and plutonic chromites from Pagé et al. (2016).*

Chromites from other intrusions are generally less enriched in PGEs, with chromites from the Lunar Creek intrusion generally having the lowest PGE concentrations and potentially reflecting the high abundance of PGM inclusions. The extent of intrasample variability and lack of dependence on FeO^{TOT} suggests that these elements are either: 1) distributed very heterogeneously during the initial crystallization of chromite, possibly as a result of heterogeneous melt distribution, or nano-nugget nucleation or 2) that they are highly mobile in chromite following crystallization. Future work will examine, in detail, the petrographic context (e.g., Webb, 2023) of trace element variation in chromite and attempt to use chromite to extract information about intrinsic properties of Alaskan-type parental magmas. This may include quantifying $f(O_2)$ using V_2O_3 concentrations and V/Sc of chromites (e.g., Canil, 2002) and using olivine-spinel pairs to quantify both magmatic temperatures and $f(O_2)$ (e.g., Ballhaus et al., 1991; Zhang et al., 2023). The results of this and future studies will be used to understand the intrinsic properties of primitive arc magmas and processes that govern the formation of Ni-Cu-PGE-rich magmatic deposits in convergent margin settings.

SUMMARY

This report contains chromite compositions, determined by Electron Probe Microanalysis (EPMA) and Laser Ablation-Inductively Coupled Plasma-Mass Spectrometry (LA-ICP-MS), from Tulameen, Polaris, Dortatelle Creek, Wrede Creek, Lunar Creek and Turnagain Alaskan-type ultramafic-mafic intrusions in British Columbia. Chromite compositions show significant heterogeneity that reflects variable post-crystallization re-equilibration and metamophism of Cr-rich grains formed from ultramafic magmas with arc affinity. This data will aid in the ongoing effort to better constrain the intrinsic petrological properties of magmas parental to Alaskan-type intrusions, their ability to transport critical metals across the mantle-crust interface and, to evaluate their economic potential.

DATA

Scanning Electron Microscope images and locations of individual spot analyses are presented in Electronic Appendix 1. LA-ICP-MS maps are presented in Electronic Appendix 2. Complete EPMA and LA-ICP-MS data for individual spot analyses is provided in electronic Appendices 3 and 4-5, respectively.

ACKNOWLEDGMENTS

This research is funded by the Geological Survey of Canada's TGI-6 program. We thank the Tsay Keh Dene and Kwadacha First Nations for being supportive of our fieldwork and Benchmark Metals, Apex Geoscience, and SilverKing Helicopters for logistical support in 2022. J. Czas provided a thorough and constructive review.

REFERENCES

Ballhaus, C., Berry, R.G., and Green, D.H., 1991. High pressure experimental calibration of the olivine-orthopyroxene-spinel oxygen geobarometer: implications for the oxidation state of the upper mantle. Contributions to Mineralogy and Petrology **107**, 27–40.

Barnes, S.J. and Roeder, P.L., 2001. The range of spinel compositions in terrestrial mafic and ultramafic rocks. Journal of Petrology **42**, 2279-2302.

Barnes, S.-J., Pagé, P., Prichard, H.M., Zientek, M.L. and Fisher, P.C., 2016. Chalcophile and platinum-group element distribution in the Ultramafic series of the Stillwater Complex, MT, USA—implications for processes enriching chromite layers in Os, Ir, Ru, and Rh. Mineralum Deposita **51**, 25-47.

Barnes, S.-J., Mansur, E.T., and Pagé, P., 2022. Differences in composition from low-Ti and high-Ti picrites of the Emeishan LArge Igneous Province and comparison with chromites of the UG-2 platinum-deposit of the Bushveld complex. Lithos **412-413**, 1066613.

Barnes, S.-J., Mansur, E.T., Maier, W.D., and Prevec, A., 2023. A comparison of trace element concentrations from komatiites, picrites, and layered intrusions: implications for the formation of massive chromite layers. Canadian Journal of Earth Sciences **60**, 97-132.

Bédard, J.H. and Hébert, R., 1998. Formation of chromitites by assimilation of crustal pyroxenites and gabbros into peridotitic intrusions: North Arm Mountain massif, Bay of Islands ophiolite, Newfoundland, Canada. Journal of Geophysical Research **103**, 5165–5184.

Canil, D. 2002. Vanadium in peridotites, mantle redox and tectonic environments: Archean to Present: Earth and Planetary Science Letters **195**, 75-90.

Colás, V., González-Jiménez, J.M., Griffin, W.L., Fanlo, I., Gervilla, F., O'Reilly, S.Y., Pearson, N.J., Kerestedjian, T., and Proenza, J.A. 2014. Fingerprints of metamorphism in chromite: New insights from minor and trace elements. Chemical Geology **389**, 137-152.

Davis, F.A., Cottrell, E., Birner, S.K., Warren, J.M. and Lopez, O.G., 2017. Revisiting the electron microprobe method of spinel-olivine-orthopyroxene oxybarometry applied to spinel peridotites. American Mineralogist **102**, 421-435.

Droop, G.T.R., 1987. A general equation for estimating Fe^{3+} concentrations in ferromagnesian silicates and oxides from microprobe analyses, using stoichiometric criteria. Mineralogical Magazine **51**, 431–435.

Eales, H.V. and Reynolds, I.M., 1986. Cryptic variations within chromitites of the upper critical zone, northwestern Bushveld complex. Economic Geology **81**, 1056–1066.

Garuti, G., Pushkarev, E.V., Zaccarini, F., Cabella, R., & Anikina, E., 2003. Chromite composition and platinum- group mineral assemblage in the Uktus Uralian-Alaskan-type complex (Central Urals, Russia). Mineralium Deposita **38**, 312–326.

Guillong, M., Hametner, K., Reusser, E., Wilson, S.A. and Günther, D. 2005. Preliminary characterisation of new glass reference materials (GSA-1G, GSC-1G, GSD-1G and GSE-1G) by laser ablation- inductively coupled plasma-mass spectrometry using 193 nm, 213 nm and 266 nm wavelengths. Geostandards and Geoanalytical Research **29**, 315-331.

Hodel, F., Macouin, M., Trindade, R.I.F., Araujo, J.F.D.F., Respaud, M., Meunier, J.F., Cassayre, L., Rousse, S., Drigo, L., and Schorne-Pinto, J., 2020. Magnetic properties of ferritchromite and Cr-magnetite and monitoring of Cr-spinels alteration in ultramafic and mafic rocks. Geochemistry, Geophysics, Geosystems **21**, e2020GC009227.

Irvine, T.N., 1965. Chromian spinel as a petrogenetic indicator: Part 1. Theory. Canadian Journal of Earth Sciences **2**, 648-672.

Jackson, S.E. 2008. LAMTRACE data reduction software for LA-ICP-MS. *in* Laser Ablation, ICP-MS in the Earth Sciences: Current practices and outstanding issues. *Edited by* P. Sylvester. Mineralogical Association of Canada Short Course Series, **vol. 40**, pp. 305-306.

Jackson-Brown, S., 2017. Origin of Cu-PGE-rich sulphide mineralization in the DJ/DB zone of the Turnagain Alaskan-type intrusion, British Columbia. Unpublished M.Sc. thesis, University of British Columbia, Vancouver, British Columbia, Canada, 272 p.

Johan, Z. 2002. Alaskan-type complexes and their Platinum- Group Element mineralization. *In* Geology, Geochemistry, Mineralogy and Mineral Beneficiation of Platinum-group Elements. *Edited by* L.J. Cabri. Canadian Institute of Mining and Metallurgy, **Special Volume 54**, pp. 669–719.

Kamentsky, V.S., Crawford, A.J., and Meffre, S., 2001. Factors controlling chemistry of magmatic spinel: an empirical study of associated olivine, Cr-spinel and melt inclusions from primitive rocks. Journal of

Petrology **42**, 655-671.

Kelemen, P., Benson, S.M., Pilorgé, H., Psarras, P., and Wilcox, J. 2019. An overview of the status and challenges of CO_2 storage in minerals and geological formations. Frontiers in Climate **1**, 9.

Lawley, C.J.M, Petts, D.C., Jackson, S.E., Zagorevski, A., Pearson, D.G., Kjarsgaard, B.A., Savard, D., and Tschirhart, V., 2000. Precious metal mobility during serpentinization and breakdown of base metal sulphide. Lithos **354-355**, 105278.

Le Bas, M.J., 2000. IUGS reclassification of the high-Mg and picritic volcanic rocks. Journal of Petrology **41**, 1467–1470.

Lee, C.-T., Leeman, W.P., Canil, D., and Li, Z.-X. A., 2005. Similar V/Sc systematics in MORB and arc basalts: implications for the oxygen fugacities of their mantle source regions. Journal of Petrology **46**, 2313-2336.

Lyubetskaya, T. and Korenaga, J., 2007. Chemical composition of Earth's primitive mantle and its variance: 1. Method and results. Journal of Geophysical Research **112**, B03211.

Milidragovic, D., Nixon, G.T., Scoates, J.S., Nott, J.A., and Spence, D.W., 2021, Redox-controlled chalcophile element geochemistry of the Polaris Alaskan-type mafic-ultramafic complex, British Columbia, Canada. Canadian Mineralogist **59**, 1627–1661.

Milidragovic, D. and Cleven, N., 2023. Field relationships indicating cumulate intermingling at the Wrede Creek and Lunar Creek Alaskan-type ultramafic- mafic intrusions, north-central British Columbia. Geological Survey of Canada, Open File **8946**, 14 p.

Nixon G.T., Cabri, L.J., Laflamme, J.H.G., 1990. Platinum-group-element mineralization in lode and placer deposits associated with the Tulameen Alaskan-type complex, British Columbia. Canadian Mineralogist **28**, 503-535.

Nixon, G.T. et al., 1997, Geology and platinum group element mineralization of Alaskan-type ultramafic-mafic complexes in British Columbia. British Columbia Ministry of Employment and Investment, British Columbia Geological Survey Bulletin **93**, 142 p.

Nixon, G.T., Manor, M.J., Jackson-Brown, S., Scoates, J.S., and Ames, D.E., 2015. Magmatic Ni-Cu-PGE sulphide deposits at convergent margins. *in* Targeted Geoscience Initiative 4: Canadian Nickel-Copper-Platinum Group Elements - Chromium Ores Systems, Fertility, Pathfinders, New and Revised Models. Edited by D.E. Ames and M.G. Houlé. Geological Survey of Canada, Open File **7856**, p. 17-34.

Nixon, G.T., Scheel, J.E., Scoates, J.S., Friedman, R.M., Wall, C.J., Gabites, J., and Jackson-Brown, S., 2020a. Syn-accretionary multi-stage assembly of an Early Jurassic Alaskan-type intrusion in the Canadian Cordillera: U-Pb and $^{40}Ar/^{39}Ar$ geochronology of the Turnagain ultramafic-mafic intrusive complex, Yukon-Tanana terrane. Canadian Journal of Earth Sciences **57**, 575–600.

Nixon, G.T., Scoates, J.S., Milidragovic, D., Nott, J., Moerhuis, N., Ver Hoeve, T.J., Manor, M.J., and Kjarsgaard, I.M., 2020b. Convergent margin Ni-Cu-PGE-Cr ore systems: U-Pb petrochronology and environments of Cu-PGE vs. Cr-PGE mineralization in Alaskan-type intrusions (W. Bleeker & M. G. Houlé, Eds.). Geological Survey of Canada, Open File **8722**, p. 197–218.

Nott, J., Milidragovic, D., Nixon, G.T., and Scoates, J.S., 2020. New geological investigations of the Early Jurassic Polaris ultramafic-mafic Alaskan-type intrusion, north-central British Columbia. Geological Fieldwork 2019, British Columbia Ministry of Energy, Mines, and Petroleum Resources, **Paper 2020-01**, p. 59–76.

Ootes, L., Bergen, A.L., Milidragovic, D., Jones, G.O., Camacho, A., and Friedman, R., 2020. An update on the geology of northern Hogem batholith and its surroundings, north-central British Columbia. Geological Fieldwork

2019, British Columbia Ministry of Energy, Mines, and Petroleum Resources, **Paper 2020-01**, p. 25–47.

Pagé, P., Bédard, J. H., Schroetter, J.-M., and Tremblay, A., 2008. Mantle petrology and mineralogy of the Thetford Mines Ophiolite Complex. Lithos **100**, 255-292.

Pagé, P. and Barnes, S.-J., 2016. The influence of chromite on osmium, iridium, ruthenium and rhodium distribution during early magmatic processes. Chemical Geology **420**, 51-68.

Palme, H. and O'Neill, H.ST.C., 2003. Cosmochemical estimates of mantle composition. *in* Treatise on Geo- chemistry, Vol. 2 (H.D. Holland & K.K. Turekian, Eds.). Elsevier, Amsterdam, The Netherlands, p. 1–38.

Pearce, J.A. and Reagan, M.K., 2019. Identification, classification, and interpretation of boninites from Anthropocene to Eoarchean using Si-Mg-Ti systematics. Geosphere **15**, 1008– 1037.

Power, I.M., Dipple, G.M., Bradshaw, P.M.D., and Harrison, A.L., 2020. Prospects for CO_2 mineralization and enhanced weathering of ultramafic mine tailings from the Baptiste nickel deposit in British Columbia, Canada. International Journal of Greenhouse Gas Control **194**, 102895

Smith J., Bleeker W., and Petts D.C., 2022. Distribution of siderophile elements during sulphide fractionation within magmatic Ni-Cu-PGE systems: A LA-ICP-MS investigation of the Crystal Lake Intrusion, 1.1 Ga Midcontinent rift. Ore Geology Reviews **148**, 105002.

Smith J., Graziani R., Petts D.C. and Regis D., 2023. Crystallographic controlled exsolution and metal partitioning in magmatic sulfide deposits. Geochemistry **83**, 125954.

Sylvester, P.J, C, Cabri, L.J., Tubrett, M.N., McMahon, G., Laflamme J.H.G and Peregoedova, A. 2005. Synthesis and evaluation of a fused pyrrhotite standard reference material for platinum group element and gold analysis by laser ablation-ICP-MS. *in* 10th International Platinum Symposium: Oulu, Geological Survey of Finland, Extended Abstracts *(*T.O. Törmänen and T.T. Alapieti, Eds.), p. 16–20

Webb, RE., 2023. Petrochemistry of chromite in the Polaris and Tulameen Alaskan-type ultramafic-mafic intrusions of British Columbia, Canada. Unpublished B.Sc. Hons. thesis, University of British Columbia, Vancouver, British Columbia, Canada, 149 p.

Zhang, Y., Namur, O., Li, W., Shorttle, O., Gazel, E., Jennings, E., Thy, P., Grove, T.L., and Charlier, B., 2023. An extended calibration of the olivine-spinel aluminum exchange thermometer: application to the melting conditions and mantle lithologies of large igneous provinces. Journal of Petrology **64**, 1-28.